bioRxiv preprint doi: https://doi.org/10.1101/2021.10.01.462690; this version posted October 1, 2021. The copyright holder for this preprint (which was not certified by peer review) is the author/funder, who has granted bioRxiv a license to display the preprint in perpetuity. It is made available under aCC-BY-ND 4.0 International license.

Topographic connectivity and cellular profiling reveal detailed input pathways and functionally distinct cell types in the subthalamic nucleus

Hyungju Jeon[1,6], Hojin Lee[1,2,6], Dae-Hyuk Kwon[3], Jiwon Kim[1,2], Keiko Tanaka-Yamamoto[1,2], Linqing Feng[1], Hyeran Park[4], Yong Hoon Lim[5], Zang-Hee Cho[3], Sun Ha Paek[5], and Jinhyun Kim[1,2,*]

[1]Center for Functional Connectomics, Korea Institute of Science and Technology (KIST), Seoul, 02792, Korea. [2]Division of Bio-Medical Science & Technology, KIST-School, University of Science and Technology, Seoul, 02792, Korea. [3]Neuroscience Convergence Center, Korea University, Seoul, 02841, Korea. [4]Soonchunhyang University Seoul Hospital, Seoul, 04401, Korea. [5]Neurosurgery, Movement Disorder Center, Seoul National University College of Medicine, Advanced Institute of Convergence Technology (AICT), Seoul National University, Seoul, 03080, Korea

[6]H.J., and H.L. contributed equally to this work.

[*]To whom correspondence may be addressed: Jinhyun Kim (jinnykim@me.com).

Center for Functional Connectomics (CFC), L7-7211, Brain Science Institute at the Korea Institute of Science & Technology (KIST), 39-1 Hawolgokdong, Seongbukgu, Seoul 02792, Korea; phone: +82-2-958-7225

Further information and requests for resources and reagents should be directed to and will be fulfilled by the lead contact, Jinhyun Kim (jinnykim@me.com).

bioRxiv preprint doi: https://doi.org/10.1101/2021.10.01.462690; this version posted October 1, 2021. The copyright holder for this preprint (which was not certified by peer review) is the author/funder, who has granted bioRxiv a license to display the preprint in perpetuity. It is made available under aCC-BY-ND 4.0 International license.

Summary: The subthalamic nucleus (STN) controls psychomotor activity and is an efficient therapeutic deep brain stimulation target in Parkinson's disease patients. Despite evidence indicating position-dependent therapeutic effects and distinct functions within the STN, input circuit and cellular profile in the STN remain largely unclear. Using advanced neuroanatomical techniques, we constructed a comprehensive connectivity map of the indirect and hyperdirect pathways in both the mouse and human STN. Our detailed circuit- and cellular-level connectivity revealed a topographically graded organization with three convergent types of indirect and hyperdirect-pathways. Furthermore, we identified two functional types of glutamatergic STN neurons (parvalbumin, PV +/- neurons) segregated with a topographical distribution. Glutamatergic PV+ STN neurons contribute to burst firing. We confirmed synaptic connectivity from indirect and hyperdirect pathways to both PV+ and PV-. These data suggest a complex interplay of information integration within the basal ganglia underlying coordinated movement control and therapeutic effects.

Keywords: Subthalamic nucleus; connectivity; indirect and hyperdirect pathways; cell type; firing pattern;

bioRxiv preprint doi: https://doi.org/10.1101/2021.10.01.462690; this version posted October 1, 2021. The copyright holder for this preprint (which was not certified by peer review) is the author/funder, who has granted bioRxiv a license to display the preprint in perpetuity. It is made available under aCC-BY-ND 4.0 International license.

Introduction

The subthalamic nucleus (STN), a key element of the basal ganglia (BG), plays a central role in psychomotor control and serves as the most efficient therapeutic target of deep brain stimulation (DBS) in Parkinson's disease patients (Benabid et al., 2009; Bergman et al., 1990; Bevan, 2017; Eisenstein et al., 2014; Group, 2001; Herzog et al., 2004; Kopell et al., 2006; Limousin et al., 1995; Lozano and Lipsman, 2013). Within the STN, two principal tracts modulate the activity of the BG: the indirect and hyperdirect pathways. The indirect pathway carries most GABAergic inputs to the STN from external globus pallidus (GPe) neurons (Mallet et al., 2012; Smith et al., 1998), while the hyperdirect pathway carries most glutamatergic inputs to the STN (**Figure 1A**) (Monakow et al., 1978; Nambu et al., 2002; Smith et al., 1998). The balance of synaptic excitation and inhibition is critical to the operation of brain microcircuits, and this balance is often perturbed in diseases (Chu et al., 2017; Cobos et al., 2005; del Pino et al., 2013; Fan et al., 2012; Kopell et al., 2006; Turrigiano, 2011; Yizhar et al., 2011). The effects of STN DBS appear to involve an interplay of converging inhibitory indirect and excitatory hyperdirect pathways, as well as multiple interactions from molecular and cellular processes that translate into global network effects (Gradinaru et al., 2009; Hashimoto et al., 2003; Hemptinne et al., 2015; Li et al., 2012; Stefani et al., 2005; Windels et al., 2000). Although there is evidence indicating heterogeneous firing patterns, distinct functional movement control, and electrode position-dependent therapeutic effects including side-effects of DBS within the STN (Herzog et al., 2004; Kaku et al., 2019; Kim et al., 2015; Mallet et al., 2012; Mosher et al., 2021; Wodarg et al., 2012), detailed topographical profiling of connectivity, cytoarchitecture, and physiological properties remain incomplete. Thus, comprehensive information regarding these input patterns as well as cellular profiles of the STN is critical for deepening our understanding of normal movement control, Parkinson's disease, and DBS. Here, using advanced neuroanatomical techniques, we developed detailed three-dimensional (3D) descriptions of the convergent connectivity in the indirect and hyperdirect pathways, as well as molecular and cellular profiles of STN circuitry. Our analysis includes a

bioRxiv preprint doi: https://doi.org/10.1101/2021.10.01.462690; this version posted October 1, 2021. The copyright holder for this preprint (which was not certified by peer review) is the author/funder, who has granted bioRxiv a license to display the preprint in perpetuity. It is made available under aCC-BY-ND 4.0 International license.

comparison of ultrahigh-resolution fiber tractography in the human STN with respect to the effectiveness of STN DBS in Parkinson's disease patients. Our circuit-level connectivity revealed a topographically graded organization, with overlaps and no evident anatomical boundaries, and direct cortico-pallidal connection in both the mouse and human STN. Together with cellular-level connectivity analysis, we found, at least, three convergent types of indirect and hyperdirect-pathway (GPe-only, STN-only, and both) suggesting complex signal integration, such as a classical convergence of inhibition and excitation, feedforward inhibition, and collateral convergence. These circuit features imply functional computational complexity and delicate control. Furthermore, we identified two functional types of glutamatergic STN parvalbumin (PV) +/- neurons that integrate information from both indirect and hyperdirect pathways, are segregated along a topographical distribution. Glutamatergic PV+ neurons show phasic burst firing and are particularly prevalent in the dorsolateral and middle STN, whereas PV- neurons fail to generate burst firing and prevalent in the ventromedial and middle STN. In addition, we confirmed synaptic connectivity from indirect and hyperdirect pathways to PV+/- neurons by combining retrograde virus injections and mammalian GFP reconstitution across synapses (mGRASP) (Kato et al., 2014; Kim et al., 2012). Our analysis corrects errors and adds a critical new level of detail to understanding STN circuitry.

bioRxiv preprint doi: https://doi.org/10.1101/2021.10.01.462690; this version posted October 1, 2021. The copyright holder for this preprint (which was not certified by peer review) is the author/funder, who has granted bioRxiv a license to display the preprint in perpetuity. It is made available under aCC-BY-ND 4.0 International license.

Results

Indirect pathway in the STN

To comprehensively analyze the organization of the indirect pathway in the mouse STN (IP_{STN}), we employed a mesoscopic approach with the following components: 1) topographic labeling of subsets of GPe neurons with adeno-associated virus (AAV) expressing green or red fluorescent proteins (sfGFP or tdTomato), 2) computational reconstruction of axonal projection patterns, and 3) connecto-informatics of the GPe-STN circuit (**Figure 1; Figure S1–3;** see **STAR Methods**). To obtain IP_{STN} data, we conducted 73 injections into the GPe, serially imaged the GPe and STN, and then aligned our images to the Allen Mouse Brain Common Coordinate Framework (CCF v3, https://mouse.brain-map.org; **Figure 1A; Figure S1A; Movie S1**). After filtering our data to remove artifactual and weak projection signals, the results from 55 injections covering 84% of the GPe volume were further analyzed for IP_{STN} patterns (**Figure 1B; Figure S1B, C; Table S1**). Injections and axonal projections were reconstructed onto the segmented GPe and STN, respectively (**Figure S2**).

To investigate IP_{STN} connectivity patterns, we constructed heatmaps of GPe injection and STN projection (IP_{STN}) distributions along the whole-brain anatomic axes, that is, anterior-posterior (AP), medial-lateral (ML), and dorsal-ventral (DV; **Figure 1C; Figure S3A, B**). The centrality of the signal distribution was used to identify injection and projection sites, and to subsequently measure their correlation. These heatmaps show that while projection signals were dispersed throughout the STN, injection signals were restricted to specific topographic loci in the GPe, which is desirable for fine connectivity mapping. Reconstructed STN projection patterns show a graded distribution with a notable degree of overlap, rather than divisible sub-territories (**Figure 1C–E; Figure S2, 3**) (Lambert et al., 2012; Mallet et al., 2007; Parent and Hazrati, 1995; Plantinga et al., 2018). This gradient was predominantly oriented along the ventromedial to dorsolateral axis, corresponding with the geometric longitudinal axis of the STN, termed “STN axis1”, and also along the transverse direction, perpendicular to the longitudinal axis, termed

bioRxiv preprint doi: https://doi.org/10.1101/2021.10.01.462690; this version posted October 1, 2021. The copyright holder for this preprint (which was not certified by peer review) is the author/funder, who has granted bioRxiv a license to display the preprint in perpetuity. It is made available under aCC-BY-ND 4.0 International license.

"STN axis2" (**Figure 1D, and 1F**). Although the centroid-based measurement effectively represents the projection sites, it may not fully portray the varying spatial pattern of broadly dispersed axonal projections. Therefore, we used multidimensional scaling (MDS) that visualizes the level of similarity of projection patterns in a 3D space, termed "pattern space" (see **STAR Methods**). Projections in a pattern space generated by MDS were continuously arranged with little or no noticeable segregation along two major dimensions which were significantly correlated with the STN axes (**Figure 1G**). Consistent with the centroid analysis, MDS confirmed graded topographic organization of IP_{STN} along the geometrical axes of the STN (STN axes 1 and 2). We then investigated the topographic relationships between inputs originating in the GPe and their projection targets by pairwise comparison of each GPe input locus and its corresponding projection locus in the STN along STN axes 1 and 2. Our analysis of input and projection distributions in the indirect pathway indicated that injection sites in the GPe are topographically aligned linearly along two directions, matching the geometric longitudinal and transverse axes of the GPe itself (**Figure 1H;** see **STAR Methods**). Interestingly, along STN axis2, the input-projection pattern was reversely related, revealing a "cross-over" projection pattern from the GPe to the STN. Our detailed analysis of GPe-STN connectivity clearly shows graded IP_{STN} organization along geometric axes, with generally extensive overlaps and an absence of sharp boundaries.

Hyperdirect pathway in the STN

Next, to comprehensively assess the organization of the hyperdirect pathway in the STN (HP_{STN}), we extracted data from the Allen Mouse Brain Connectivity Atlas dataset (AMBCA, https://connectivity.brain-map.org) (Oh et al., 2014) regarding axonal projections following isocortical injections. Our data-filtering criteria included detectable STN projection signals and contamination of cortical injection (**Figure 2A; Figure S1A and 4A–C;** see **STAR Methods**). The resulting dataset included 176 injections with AAV-expressing fluorescent proteins throughout the isocortex, covering 71% of the volume of layer (L) 5 in wild-type C57BL/6J mice and nine

bioRxiv preprint doi: https://doi.org/10.1101/2021.10.01.462690; this version posted October 1, 2021. The copyright holder for this preprint (which was not certified by peer review) is the author/funder, who has granted bioRxiv a license to display the preprint in perpetuity. It is made available under aCC-BY-ND 4.0 International license.

transgenic Cre lines shown to have L5-specific expression of Cre (**Figure 2B; Table S2, 3**). Additionally, our own retrograde tracer experiments using retro-AAV or -Lenti systems (Kato et al., 2014; Tervo et al., 2016) confirmed that HP_{STN} arises in various cortical subregions, mainly from a subpopulation of corticofugal neurons in the ipsilateral L5, which is consistent with previous observations (Kita and Kita, 2012) (**Figure S4D**).

Information flow from the cortex to the BG is believed to progress through a hierarchical series of sensorimotor, association, and limbic areas, supporting the tripartite STN model (Lambert et al., 2012; Mallet et al., 2007; Parent and Hazrati, 1995; Plantinga et al., 2018). However, much of the data leading to this view regarding the subdivisions of the STN are qualitative, variable, fragmented, and difficult to reconcile, owing to the technical limitations of neuroanatomical research (Alkemade and Forstmann, 2014; Keuken et al., 2012; Lambert et al., 2015). Therefore, to update this view of the STN, we first performed an inclusive analysis at the level of region-to-region connectivity of the HP_{STN}. We found that STN projection patterns from each cortical subregion exhibited distinct yet extensively overlapping projection patterns (**Figure 2C**). For instance, projections from motor cortical areas such as the primary and secondary motor areas (MOp and MOs) broadly targeted the center region of the STN, while those from sensory areas such as primary and supplemental somatosensory areas (SSp and SSs) targeted the dorsolateral STN (anatomic abbreviations and functional groups shown in **Table S2**). Association areas, such as the retrosplenial (RSP), visual (VIS), and visceral (VISC) area, and limbic areas, such as anterior cingulate (ACA) and orbital (ORB) area, contained dorsolateral and ventromedial STN projections spanning the central part of STN, respectively. Overall, our analysis of STN projection patterns showed much broader coverage, with more extensive overlap than previously thought (Lambert et al., 2012; Mallet et al., 2007; Parent and Hazrati, 1995; Plantinga et al., 2018). Furthermore, within motor and sensory cortices, we found that individual injections revealed variable and distinct yet overlapping projections in the STN (**Figure 2D**). Hence, we investigated the organization of the HP_{STN} using non-biased techniques, such as a voxel-based analysis that disregards anatomically defined cortical subregions. Similar to our analysis of the

bioRxiv preprint doi: https://doi.org/10.1101/2021.10.01.462690; this version posted October 1, 2021. The copyright holder for this preprint (which was not certified by peer review) is the author/funder, who has granted bioRxiv a license to display the preprint in perpetuity. It is made available under aCC-BY-ND 4.0 International license.

IP_{STN} described above, we examined the distributions of cortical inputs and STN projections along the whole-brain anatomic axes (AP, ML, and DV). We found that the HP_{STN} had a graded distribution with a notable degree of overlap along STN axis1 (**Figure 2E**). Furthermore, MDS analysis indicated that the 3D projection patterns of the HP_{STN} were gradually distributed along STN axis1 and axis2 (**Figure 2F**). Together, these results indicate that the HP_{STN} has graded organization along geometric axes, with overlaps and an absence of sharp boundaries, which prompts re-evaluation of the conventional view of a functionally subdivided STN determined by cortical input patterns.

Hyperdirect pathway in the GPe

We expanded our analysis of the hyperdirect pathway to include projection patterns in the GPe. Based on previous reports (Abecassis et al., 2020; Karube et al., 2019; Naito and Kita, 1994; Winnubst et al., 2019) showing the existence of direct cortico-pallidal connections, we questioned whether the hyperdirect pathway providing direct cortico-pallidal projections into the GPe (called HP_{GPe}) collaterally provides HP_{STN}, and how HP_{GPe} displays topographic distributions. First, we injected retro-AAV-iCre and Cre-dependent AAV-JxON-tdTomato into the GPe and MOp, respectively, and then cleared the tissue. Our results revealed strong collateral projections from labeled MOp neurons in both the GPe and STN with additional downstream targets in the substantia nigra (SN) and superior colliculus (SC), but few or no targets in contralateral cortical areas (**Figure 3A**). As with the HP_{STN}, we observed graded organization within the HP_{GPe}. The HP_{GPe} appeared to be topographically organized with fidelity to the whole-brain anatomic axes and segmented into a tripartite form. This was especially the case with respect to inputs arising in association and limbic areas, which is comparable to the HP_{STN} (**Figure 3B**). This organization might arise through the innate geometric situation of the GPe matched with the whole-brain anatomic axes and/or the larger receptive volume of the GPe compared with the STN. Next, we conducted pairwise topographic matching between the loci of cortical inputs and projections in the GPe (HP_{GPe}). We found two major axes of topographic organization of hyperdirect pathway inputs

bioRxiv preprint doi: https://doi.org/10.1101/2021.10.01.462690; this version posted October 1, 2021. The copyright holder for this preprint (which was not certified by peer review) is the author/funder, who has granted bioRxiv a license to display the preprint in perpetuity. It is made available under aCC-BY-ND 4.0 International license.

and the HP_{GPe} that were correlated and reversely correlated along STN axis1 and axis2, respectively (**Figure 3C, D; Figure S5A**). These gradient axes of the HP_{GPe} appeared to match the geometric axes of the GPe, which is similar to the gradient axes observed for input into the indirect pathway. To examine the relationship between the two pathways along these gradient axes, we performed a paired comparison between the IP and HP patterns. For this analysis, we measured the similarity between the pathways in the STN and GPe, respectively. The HP_{STN} and IP_{STN} projection patterns were used to examine the gradient similarity in the STN, while the HP_{GPe} and indirect pathway input (IP_{INPUT}) were used for that in the GPe. We then calculated the correlation between these pairwise similarities in the STN and GPe. We found strong similarities in STN projection patterns between the IP_{STN} and HP_{STN} when the IP_{INPUT} and HP_{GPe} locus were located close together (**Figure 3E**).

Complex integration of the indirect and hyperdirect pathways in the STN

Given our findings that the IP_{STN}, HP_{STN}, and HP_{GPe} are topographically organized with gradient convergence at the mesoscopic level, we next performed a detailed analysis of HP connectivity at the cellular level. To dissect HP connectivity types, we first labeled cortical neurons innervating HP_{STN} and/or HP_{GPe} by injecting retro-AAV-tdTomato and -sfGFP in the STN and GPe, respectively. We identified three types of cortical neurons in L5 of MOp: Those innervating only HP_{STN}, only HP_{GPe}, and both $HP_{GPe/STN}$ (**Figure 3F**). Additionally, by data-mining single-neuron reconstruction data from the MouseLight project (http://www.mouselight.janelia.org) (Winnubst et al., 2019), we confirmed the existence of these three types of cortical neurons (**Figure 3G; Figure S5B, C**). Neurons innervating the HP_{STN} are predominantly pyramidal tract (PT) neurons, while those innervating the HP_{GPe} are both PT and intratelencephalic (IT) neurons, with a subset (~15 %) that collaterally innervate the $HP_{GPe/STN}$. Notably, the axonal density of neurons innervating the $HP_{GPe/STN}$ in the STN is 3.7-fold higher than that in the GPe. Consistent with our mesoscopic retrograde tracer data, shown in **Figure 3A**, we found that cortical neurons innervating the $HP_{GPe/STN}$ send collateral innervations to multiple brain areas such as the striatum

bioRxiv preprint doi: https://doi.org/10.1101/2021.10.01.462690; this version posted October 1, 2021. The copyright holder for this preprint (which was not certified by peer review) is the author/funder, who has granted bioRxiv a license to display the preprint in perpetuity. It is made available under aCC-BY-ND 4.0 International license.

(STR), SN, SC, and others, which suggests that these neurons may help orchestrate movement. Although we analyzed a small set of reconstructed single neurons, their projection patterns were consistent with our mesoscopic, topographic analysis of the HP_{GPe} and HP_{STN} (**Figure S5D**). Our results indicate that at least three types of signals from the indirect and hyperdirect pathways in the STN are integrated, including a classical form of convergence of inhibition and excitation, feedforward inhibition, and collateral convergence (parallel after-discharge-like circuitry; **Figure 3H**). In addition, we confirmed HP projections into the human STN at the macroscopic scale by 7T-MRI-based *in vivo* ultrahigh-resolution fiber tractography of a healthy human brain (**Figure S6; Table S4**; see **STAR Methods**). Our seed-based probabilistic tractography of the HP revealed a direct cortico-pallidal connection, the HP_{GPe}, and a collateral $HP_{GPe/STN}$ in the human brain, similar to those we observed in mice (**Figure S6B, C**). We divided cortical subregions into three groups: motor, limbic, and association (further divided into prefrontal- and rest-association) areas (**Table S2**). HP projections from the association, motor, and limbic areas were only somewhat segregated in the ventromedial, dorsolateral, and ventrolateral areas, respectively, appearing along the longitudinal axis of the STN (axis1). However, as we observed in the mouse HP_{STN}, there was a high degree of overlap and no evident anatomical borders or clear subdivisions (**Figure S7D–H**). We also found the HP_{STN}, HP_{GPe}, and collateral $HP_{GPe/STN}$ organization in the human brain to be consistent with the complex signal integration patterns in the mouse. In agreement with our mouse connectivity maps, our analysis of human 7T MRI-based tractography data revealed considerable and gradual overlap along the longitudinal axis of the human STN. Together, these results suggest that graded convergence of IP_{STN} and HP_{STN} is organized along the STN geometric axes, and that GPe neurons innervating the IP_{STN} might be activated by the same HP_{STN}. These circuit features imply functional computational complexity and delicate control, updating classical models (DeLong and Wichmann, 2015) with the idea that the indirect and hyperdirect pathways participate in relaying and integrating information needed for coordinated movement.

bioRxiv preprint doi: https://doi.org/10.1101/2021.10.01.462690; this version posted October 1, 2021. The copyright holder for this preprint (which was not certified by peer review) is the author/funder, who has granted bioRxiv a license to display the preprint in perpetuity. It is made available under aCC-BY-ND 4.0 International license.

Cellular composition of the STN

The way in which STN neurons process convergent inputs from the IP and HP depends critically on the molecular and cellular properties of these neurons. The STN is generally described as a homogenous glutamatergic nucleus of the BG. To test this, we used serial single-molecule fluorescence in situ hybridization (smFISH) with a custom computational analysis for cell-type markers and receptors to examine the topographic molecular and cellular profile of the STN (**Figure 4A**; see **STAR Methods**). Most STN neurons identified by the neuronal marker *Rbfox3* co-expressed the glutamatergic marker *Slc17a6*, while very few neurons co-expressed the GABAergic marker *Slc32a1*. Approximately half of the STN cells expressed glia-associated genes (*Aqp4*, *Mbp*, and *Tmem119*) (**Figure S7**). Thus, our serial smFISH, immunostaining, and topographic analysis confirmed that most neurons in the STN are purely glutamatergic. Previous anatomical studies have reported the presence of parvalbumin-expressing (PV+) neurons in the STN (Alkemade et al., 2019; Hontanilla et al., 1998; Lévesque and Parent, 2005; Wu et al., 2018). PV expression is conventionally interpreted to reflect a GABAergic subpopulation (Hu et al., 2014), which is inconsistent with our serial smFISH results and previous studies (Lévesque and Parent, 2005; Roccaro-Waldmeyer et al., 2018). Accordingly, we conducted detailed cellular characterization of PV+ STN neurons. First, we performed triple smFISH for *Pvalb*, *Slc17a6*, and *Slc32a1*. We found that *Pvalb*+ neurons in the STN exclusively co-express glutamatergic marker *Slc17a6*, but not GABAergic marker *Slc32a1*, whereas those in the other brain areas such as hippocampus, cortex, and zona incerta co-express *Slc32a1* (**Figure 4B–D; Figure S8A**). Notably, quantitative analysis of the topographic distribution of *Pvalb*+ neurons indicated that glutamatergic PV+ neurons were particularly prevalent in the dorsolateral and middle STN (**Figure 4C, D**). Our serial multiplex-smFISH data provide direct evidence that PV+ STN cells are glutamatergic with topographic segregation in the STN (Hontanilla et al., 1998; Wu et al., 2018) and suggest that parvalbumin cannot reliably serve as a marker for GABAergic interneurons, together with previous findings (Jinno and Kosaka, 2004; Shang et al., 2015; Wallace et al., 2017).

bioRxiv preprint doi: https://doi.org/10.1101/2021.10.01.462690; this version posted October 1, 2021. The copyright holder for this preprint (which was not certified by peer review) is the author/funder, who has granted bioRxiv a license to display the preprint in perpetuity. It is made available under aCC-BY-ND 4.0 International license.

To examine further physiological properties of PV+ STN neurons, we used PV-IRES-Cre::Ai6 mice expressing ZsGreen in PV+ cells. We first confirmed that PV+ neurons in the STN of these mice were immunohistochemically positive for glutamate and negative for GABA (**Figure 5A**). By clearing parasagittal sections (2.5 mm in thickness) that embrace the entire STN without making physical cuts, we 3D-mapped total PV+ neurons in the STN and found topographically segregated distribution in the dorsolateral and middle STN, consistent with serial-smFISH data (**Figure 5B; Movie S2**). Because Parkinsonian symptoms are correlated with an increase in burst firing in STN neurons, we next recorded the firing patterns of glutamatergic PV+/- STN neurons using PV-IRES-Cre::Ai6 mice. Both PV+ and PV− neurons displayed similar spontaneous firing and other basic properties including input resistance (**Table S5**). However, only PV+ neurons showed phasic burst firing, which we refer to a firing pattern, composing of fast firing (an interspike interval, ISI, of less than 10 ms) and a pause; even current injection could not evoke bursts from PV− neurons (**Figure 5C-F; Figure S8B-E; Table S6;** see **STAR Methods**). Burst and tonic firing patterns were observed at an equivalent membrane potential range (-58 to -45 mV) (**Figure S8E**), suggesting that burst firing was not due to differences in the membrane potential *per se*, even though firing patterns in STN neurons can be affected by membrane potentials (Kass and Mintz, 2006). Injection of negative current pulses evoked significantly smaller hyperpolarization-induced depolarizing sags in PV+ vs. PV− neurons, which was consistent with their burst properties (**Figure 5F**). Taken together, our results provide clear evidence that there are at least two functional types of glutamatergic neurons in the STN, and that glutamatergic PV+ neurons contribute to burst firing in the dorsolateral and middle STN. This is compatible with previous studies of spatial distribution of firing patterns by intraoperative microelectrode recording within the human STN showing the occurrence of burst firing in in the dorsal STN while tonic firings towards the ventral STN (Kaku et al., 2019).

Cell type-dependent synaptic connectivity

bioRxiv preprint doi: https://doi.org/10.1101/2021.10.01.462690; this version posted October 1, 2021. The copyright holder for this preprint (which was not certified by peer review) is the author/funder, who has granted bioRxiv a license to display the preprint in perpetuity. It is made available under aCC-BY-ND 4.0 International license.

Our analysis defined new functional cell types and established wiregrams for the IP_{STN} and HP_{STN}, allowing us to refine our analysis of synaptic connectivity in the IP and HP to be cell type-specific. Thus, we tested whether the IP_{STN} and HP_{STN} form PV+/- cell-specific synaptic connections, and whether the HP_{GPe} forms synapses on the two major GABAergic cell types in the GPe, that is, prototypic neurons projecting to the STN and arkypalidal neurons projecting to the striatum (Mallet et al., 2012; Mastro et al., 2014). By combining retrograde virus injections and mammalian GFP reconstitution across synapses (mGRASP) (Kato et al., 2014; Kim et al., 2012), which is an advanced method for accurately detecting synaptic connections, we mapped synaptic connectivity of these four cell-types in IP_{STN}, HP_{STN}, and HP_{GPe} (**Figure 6A-F**; see **STAR Methods**). We identified synaptic connections in STN PV+ and PV− neurons originating in both the IP_{STN} and HP_{STN}, by injecting AAV expressing the pre- and post-synaptic mGRASP components into the GPe (for IP_{STN}), cortex (for HP_{STN}), and STN, respectively. STN PV+/- neurons were distinguished by injection of AAV expressing iRFP in a Cre-dependent manner into the PV-Cre mouse line. We also observed synaptic connections in both GPe prototypic and arkypalidal neurons (labeled by a combination of retro-Lentivirus expressing iCre injected into the STN and STR, respectively, and AAV expressing Cre-On-postsynaptic mGRASP into the GPe) projecting from the HP_{GPe} (labeled by injecting presynaptic mGRASP in the cortex). Our analysis revealed that axonal projections in both the STN and GPe from the IP_{STN} and HP_{STN}, and from the HP_{GPe}, respectively, indeed serve as inputs. Furthermore, our results indicated that all four cell types in the STN and GPe (STN PV+, PV-, GPe arkypalidal, and prototypic neurons) communicate with each other and receive synaptic information from the cortex. Thus, in terms of cortex-GPe-STN circuitry, our data indicate that “everyone talks and everyone listens.” Next, in terms of connectivity patterns, the two types of STN neurons integrate excitatory and inhibitory signals (E/I) from the IP_{STN} and HP_{STN}. We examined the differential expression of glutamate and GABA receptors in STN PV+/- neurons. To this end, we performed serial triple smFISH for *Gria1* (encoding GluA1), *Gabra1* ($GABA_A$ α1 subunit), and *Pvalb*, and quantitatively compared their expression with respect to the topographically graded innervations of the IP_{STN} and HP_{STN} (**Figure**

bioRxiv preprint doi: https://doi.org/10.1101/2021.10.01.462690; this version posted October 1, 2021. The copyright holder for this preprint (which was not certified by peer review) is the author/funder, who has granted bioRxiv a license to display the preprint in perpetuity. It is made available under aCC-BY-ND 4.0 International license.

6G-I). Our co-expression plot of *Gria1* and *Gabra1* showed a strong correlation between these genes, indicating that most STN neurons integrate both excitatory and inhibitory inputs at the single-cell level. Notably, the total expression levels of *Gria1* and *Gabra1* formed a gradient along the STN axis1 with higher and lower expression in the ventromedial and dorsolateral STN, respectively, similar to the expression pattern of *Slc17a6* (**Figure 4C, and 6H, I**). At the cellular level, the *Gria1* to *Gabra1* expression ratio was approximately similar in the dorsolateral PV+, but this expression ratio was significantly higher in ventromedial PV− neurons (**Figure 6I**). Taken together, our results indicate that two types of glutamatergic PV+/- STN neurons, which integrate information from both the IP_{STN} and HP_{STN}, and fire in different patterns, are segregated along a topographical distribution and express different ratios of genes encoding E/I receptors. Although further direct evidence is needed, these findings may represent a step forward in characterizing the E/I imbalance of BG circuits in Parkinson's disease models, as well as the effects of DBS. Interestingly, when we analyzed DBS results with respect to electrode position within specific STN structures from 26 Parkinson's disease patients who had received bilateral STN DBS implementation together with previous studies (Herzog et al., 2004; Mallet et al., 2012; Wodarg et al., 2012), we found that patients showing DBS-associated movement improvement had electrodes placed in the dorsolateral and middle STN, with somewhat greater improvement associated with electrode placement towards the middle of STN axis1 (**Figure S9**). This part of the STN has been reported to receive direct inputs from motor cortical areas and to contain PV+ glutamatergic neurons (Alkemade et al., 2019; Eisenstein et al., 2014; Herzog et al., 2004; Lévesque and Parent, 2005; Mallet et al., 2007; Wodarg et al., 2012). The correlation among position-dependent STN DBS effects and connectivity patterns led us to hypothesize that distinct features of connectivity and cellular composition in the dorsolateral and middle STN influence the impact of DBS.

In Sum, our comprehensive profiling of circuit- and cellular-level connectivity of the indirect and hyperdirect pathways revealed a topographically graded organization with three convergent types of indirect and hyperdirect-pathway (GPe-only, STN-only, and both) in the STN.

bioRxiv preprint doi: https://doi.org/10.1101/2021.10.01.462690; this version posted October 1, 2021. The copyright holder for this preprint (which was not certified by peer review) is the author/funder, who has granted bioRxiv a license to display the preprint in perpetuity. It is made available under aCC-BY-ND 4.0 International license.

Topographically distinct molecular, cellular, and physiological properties together with the circuit features imply functional computational complexity and delicate control. Our results suggest a complex interplay of information within the basal ganglia further on than the general consensus of parallel segregated input patterns with homogeneous cytoarchitecture and physiology. Our new view of the indirect and hyperdirect pathways, cytoarchitecture, and physiology properties substantially updates classical models and suggests, from a structural basis, a way to view relayed and integrated information flow underlying coordinated movement controls and STN DBS effects (**Figure 7**).

bioRxiv preprint doi: https://doi.org/10.1101/2021.10.01.462690; this version posted October 1, 2021. The copyright holder for this preprint (which was not certified by peer review) is the author/funder, who has granted bioRxiv a license to display the preprint in perpetuity. It is made available under aCC-BY-ND 4.0 International license.

Discussion

Understanding how the STN controls motor functions, and identifying the circuit-level mechanisms underlying the effects of STN-DBS requires detailed convergent connectivity profiles for the main inhibitory and excitatory inputs in the STN. Furthermore, molecular profiles of cell types and neurotransmitter receptors in the STN are needed to infer the various interacting molecular and cellular processes that contribute to these mechanisms. In this study, we constructed a new comprehensive map of connectivity of the inhibitory indirect and excitatory hyperdirect pathways in the mouse and human STN. We identified glutamatergic PV+ STN neurons that show distinct burst firing patterns and topographical segregation in the dorsolateral and middle STN. Cell type-specific synaptic connectivity mapping revealed that both STN PV+ and PV− neurons receive synaptic inputs from both the IP_{STN} and HP_{STN} and that both GPe prototypic and arkypalidal neurons receive synaptic inputs from the HP_{GPe}. Thus, “everyone talks, and everyone listens” in cortex-GPe-STN circuitry. These data provide new insights into the basic organization of the BG network and represent an anatomic and functional guide for further dissection of BG functions and DBS effects. Detailed knowledge regarding the anatomy and connectivity pattern of cortico-BG circuits is essential for understanding the psychomotor activity and pathophysiology associated with a wide range of neurological and neuropsychiatric diseases.

The cortex is widely considered to serve as the initial input to the BG through cortico-striatal pathways that convey sensorimotor, associative, and limbic information. The information from these three functional domains is thought to be transmitted to the downstream structures of the BG in a segregated manner, which supports the tripartite model (Lambert et al., 2012; Mallet et al., 2007; Parent and Hazrati, 1995; Plantinga et al., 2018). However, our data indicate that topographically graded organization exists in both the indirect and hyperdirect pathways in the STN, with continuum overlaps, an absence of anatomical boundaries, and direct cortico-pallidal connections. Although previous studies have demonstrated that the coexistence of clearly segregated and overlapping input patterns from the cortex to the BG (Draganski et al., 2008), in

bioRxiv preprint doi: https://doi.org/10.1101/2021.10.01.462690; this version posted October 1, 2021. The copyright holder for this preprint (which was not certified by peer review) is the author/funder, who has granted bioRxiv a license to display the preprint in perpetuity. It is made available under aCC-BY-ND 4.0 International license.

the present study we constructed a large-scale map of the indirect and hyperdirect pathways, signifying a new understanding of input organization in the STN. In addition, our detailed analysis of direct cortico-pallidal connections together with recent findings regarding the complexity of the GPe (Abecassis et al., 2020; Mallet et al., 2012; Mastro et al., 2014, 2017) updates current views of the BG network, in which the GPe is considered to be a simple relay nucleus providing a unidirectional flow of information from the input structures (such as the striatum and STN) to the BG output structures (such as the GPi and SNr). These data, together with our single-cell reconstruction and cell type-specific synaptic connectivity analyses, suggest further complexity of BG functional organization through three types of information integration (**Figure 3H**), in addition to reciprocal and loop connections within the BG (Hegeman et al., 2016; Mallet et al., 2012). For instance, beyond the STN-GPe network, the hyperdirect pathway directly and/or collaterally innervates the STN and the striatum as well as two types of GABAergic GPe neurons (prototypic and arkypallidal), thus providing HP-driven feedforward inhibition. This circuit-level complexity implies the existence of anatomical substrates for precisely coordinated regulations of motor as well as nonmotor functions governed by the BG.

It is important to note that, as with any work, the present study has several potential limitations and strengths. First, at the mesoscopic level of mouse connectivity, projection signals labeled using cytosolic fluorescence proteins (FPs) include both axons from passing fibers and synaptic terminals. Like previous studies that found cytoplasmic FP signals to strongly correspond to synaptically-targeted FP signals after removing the axons of passage (Harris et al., 2019; Hunnicutt et al., 2016; Oh et al., 2014), we found no significant difference in the topographic organization of the indirect and hyperdirect pathways after removing the axons of fasciculated passing fibers observed in some areas i.e., the dorsal part of the GPe, and the anterior/posterior ends of the STN (**Figure S4E;** see **STAR Methods**). Second, to test the possibility that our discovery of a topographic gradient in the STN might be the product of graded injections, we examined a dataset showing overlapping axonal projections in the STN that were innervated from separate injections, so that no overlap in these injection sites could be

bioRxiv preprint doi: https://doi.org/10.1101/2021.10.01.462690; this version posted October 1, 2021. The copyright holder for this preprint (which was not certified by peer review) is the author/funder, who has granted bioRxiv a license to display the preprint in perpetuity. It is made available under aCC-BY-ND 4.0 International license.

guaranteed. An additional statistical analysis confirmed that neighboring yet non-overlapping injections in different functional subregions led to overlapping projection patterns in the STN (**Figure S4F**). These results support the existence of graded organization in the STN, and challenge the previous models of clear segregation, such as the tripart model. Third, at the microscopic level, although mGRASP-assisted circuit mapping provided convincing data regarding the cell types in the STN and GPe that receive synaptic inputs from the indirect and hyperdirect pathways, further fine-scale mapping of the topographic organization of convergent synaptic connectivity is necessary. Finally, for assessing human connectivity, we used diffusion-weighted image (DWI)-based tractography. This method carries some degree of inherent ambiguity, such as that related to the validity of tract reconstruction and orientation (Maier-Hein et al., 2017; Petersen et al., 2019). However, substantial scientific innovations have aimed to overcome the limitations of this technique. Regardless, it is currently the only tool for mapping human brain connectivity *in vivo,* and the data regarding overlapping patterns were highly consistent with our mouse data, which were obtained using advanced and accurate techniques, as well as with data from previous reports (Plantinga et al., 2016). Overall, our data represent a translational comparison of connectivity patterns in the STN across species.

Previous studies suggested the existence of glutamatergic PV+ neurons in STN and their topographical organization at coarse level (Hontanilla et al., 1998; Roccaro-Waldmeyer et al., 2018; Wu et al., 2018) based on immunohistochemistry with anti-PV or indirect comparison of separate conventional *in situ* hybridization datasets for PV and vGluT2, which makes it difficult to map a precise topographic distribution of STN PV+ neurons. Here, we directly identified topographically localized glutamatergic PV+ neurons in the STN using serial multiplex smFISH. They are a main contributor to burst firing, which indicates a potential key role as generators and modulators of β-band (15-30 Hz) oscillations in the BG. As excess burst firing and β-band oscillations are signatures of Parkinson's disease and these pathophysiological activities are decreased by STN DBS therapy, these burst firing PV+ STN neurons may be implicated in Parkinson's disease symptoms (Kühn et al., 2004; Steigerwald et al., 2008). By mapping the

bioRxiv preprint doi: https://doi.org/10.1101/2021.10.01.462690; this version posted October 1, 2021. The copyright holder for this preprint (which was not certified by peer review) is the author/funder, who has granted bioRxiv a license to display the preprint in perpetuity. It is made available under aCC-BY-ND 4.0 International license.

distributions of major excitatory and inhibitory transmitter receptors in the STN, we found distinct topographic patterns of expression level. These patterns suggest the existence of a functional layer of differential molecular and cellular receptibility on the top of neural connectivity. Interestingly, the E/I receptor expression ratio is equivalent in dorsolateral PV+ STN neurons, but higher in ventromedial PV- STN neurons. These results raise the important question of whether cell type-specific changes in E/I receptor expression emerge in dopamine-depleted states. Further studies designed to interrogate alterations in synaptic connectivity, receptor expression, and glutamatergic PV+ STN neuronal firing patterns in models of Parkinson's disease will provide important new insights regarding the coordinated regulation of specialized PV+ neurons in the BG network.

Our systematic connectivity maps, superimposed upon regions with distinct functional cellular heterogeneity, suggest a complex interplay of information within the BG. Our new view of the indirect and hyperdirect pathways (**Figure 7**) substantially updates classical models and proposes, from a structural basis, a new take on relayed and integrated information flow underlying coordinated movement controls and the effects of STN DBS. Further studies of other inputs (e.g. serotonergic and cholinergic) into the STN as well as its outputs will facilitate the elucidation of the mechanisms of the STN functions and complex effects of DBS.

bioRxiv preprint doi: https://doi.org/10.1101/2021.10.01.462690; this version posted October 1, 2021. The copyright holder for this preprint (which was not certified by peer review) is the author/funder, who has granted bioRxiv a license to display the preprint in perpetuity. It is made available under aCC-BY-ND 4.0 International license.

Acknowledgments

We thank members of the Kim laboratory, cooperation, and technical assistance during the course of the investigation.

Author Contributions

H.L. performed mouse connectivity experiments and imaging. H.J. performed statistical analysis with mouse connectivity. D.K. and Z.-H.C. provided and analyzed human 7T MRI data. H.L. and Jiwon Kim performed in situ hybridization and immunohistochemistry. K.T.-Y. conducted and analyzed electrophysiological data. H.J., Jiwon Kim and L.F. analyzed molecular profiling data. H.P., Y.L. and S.H.P. performed DBS surgery and collected clinical data. H.J., W.C.O., H.P., and S.H.P. analyzed DBS data. H.L., H.J., D.K., Jiwon Kim., K.T.-Y., H.P., and Jinhyun Kim wrote the original draft. All of the authors reviewed the manuscript. H.L., H.J. and Jinhyun Kim conceived and designed the study.

Competing Interest Statement

Authors declare no competing interests.

Funding

This work was supported by Korea National Research Foundation (2017M3C7A1047392), Korea Institute of Science and Technology (KIST) institutional program (2E30971), National Research Foundation of Korea (NRF) grant funded by the Korea government (MSIP) (2017M3C7A1049026), and the Samsung Science and Technology Foundation (SSTF-BA1502-11).

bioRxiv preprint doi: https://doi.org/10.1101/2021.10.01.462690; this version posted October 1, 2021. The copyright holder for this preprint (which was not certified by peer review) is the author/funder, who has granted bioRxiv a license to display the preprint in perpetuity. It is made available under aCC-BY-ND 4.0 International license.

Figure Titles and Legends

Figure 1. Graded topography of indirect pathway in STN. (A) Pipeline of indirect pathway (IP_{STN}) mapping data generation and processing. Scale bar, 250 µm. **(B)** Spatial locations (left) and coverage (right) of the GPe injections (n = 55). **(C)** Heatmap showing GPe inputs and IP_{STN} signal distribution for each injection experiment (rows) along anatomical axes (columns), sorted by the GPe injection centroid along the AP. **(D)** Illustration of STN geometric axis1 and axis2. **(E)** Heatmap of IP_{STN} and GPe inputs signal distribution, sorted by projection centroid along STN axis1. **(F)** Representative images of the GPe injection sites (left) and serial coronal images of corresponding IP_{STN} showing graded topographic organization along STN axis1 (right, top) and axis2 (right, bottom). Heatmap showing signal distribution for each slice along the white line, parallel to the corresponding STN axis. The distance from the bregma indicated at the corner. Scale bar, 250 µm. **(G)** Left: IP_{STN} projection patterns (dots) plotted in a pattern space generated via multidimensional scaling (MDS). Right: dimensions 1 and 2 in the pattern space were significantly correlated with STN axis1 and axis2 (arrows in the MDS plot), respectively (right). **(H)** Topographic organization of the IP_{STN}. Left: GPe injection sites and IP_{STN} centroids superimposed onto coronal 3D views of the GPe and STN. Colors indicate the IP_{STN} centroid location along axis1, with the corresponding GPe inputs gradient direction (arrows). Right: correlations between GPe inputs and IP_{STN} along GPe gradient axes and STN axes. Correlations were calculated via Pearson's r.

bioRxiv preprint doi: https://doi.org/10.1101/2021.10.01.462690; this version posted October 1, 2021. The copyright holder for this preprint (which was not certified by peer review) is the author/funder, who has granted bioRxiv a license to display the preprint in perpetuity. It is made available under aCC-BY-ND 4.0 International license.

Figure 2. Graded topography of hyperdirect pathway in STN. (A) Representative axonal projections in the STN (HP_{STN}) from an MOp injection (inset) extracted from AMBCA datasets. Scale bar, 250 µm. **(B)** Top: coverage (left) and spatial locations of the hyperdirect cortical injection site (right) across the isocortex (n = 176). Bottom: Bar plot of STN projection power for each subregion, an estimated STN projection volume assuming the subregion is fully labelled, shown in log-scale. Grouped functional parts of cortical subregions are color-coded (See **Table S3** for functional classification). **(C)** Digitally reconstructed serial STN projection density patterns of the averaged HP_{STN} from each grouped functional part and constituting cortical subregion at 25-µm intervals. The number in parentheses denotes the number of localized injections within the subregion. Subregions without localized injections are not shown. **(D)** Representative set of intra-subregion injections within the MO (top) and SS (bottom), and corresponding serial STN projection density at 50-µm intervals. **(E)** Heatmap showing cortical inputs and HP_{STN} signal distribution along anatomical axes (columns). Cortical injection experiments (rows) were grouped into three functional parts and sorted according to the AP of the injection centroid in each group. **(F)** Left: HP_{STN} projection patterns in the pattern space (same as in **Figure 1G**). Right: Dimensions 1 and 2 in the HP_{STN} pattern space were also significantly correlated with STN axis1 and axis2 (arrows in the MDS plot). Correlations were calculated by Pearson's r.

bioRxiv preprint doi: https://doi.org/10.1101/2021.10.01.462690; this version posted October 1, 2021. The copyright holder for this preprint (which was not certified by peer review) is the author/funder, who has granted bioRxiv a license to display the preprint in perpetuity. It is made available under aCC-BY-ND 4.0 International license.

Figure 3. Complex integration of indirect and hyperdirect pathways in STN. (A) Left: illustration of the hyperdirect pathway with a direct pallidal connection and schematic of the injection strategy for labelling collateral hyperdirect projections (retroAAV-iCre and Cre-dependent switch-on AAV-tdTomato were injected in the GPe and MOp, respectively). Right: z-projection image of a cleared parasagittal section (2.5 mm thick) showing hyperdirect projections both in the GPe and the STN, and the trajectories of the HP with two downstream targets (arrows). Scale bar, 250 µm. **(B)** Heatmap showing cortical inputs and HP_{GPe} signal distribution along anatomical axes (columns). Cortical injection experiments (rows) were grouped into three functional parts and sorted according to the AP of the injection centroid in each group. **(C)** Heatmap of sorted HP_{STN} with cortical inputs and HP_{GPe} signal distribution along the STN axis1 and corresponding cortex and GPe gradient axis. Rows are sorted by HP_{STN} axial location along STN axis1. **(D)** Left: illustration of the topographic organization of the HP_{STN}, HP_{GPe}, and cortical inputs with STN geometric axes and corresponding gradient axes of the HP_{GPe} and cortical inputs (arrows). Right: linear relationship between axial locations of the HP_{GPe} (top), HP_{STN} (bottom), and cortical inputs. **(E)** Topographic relationship between the IP and HP. Left: the projection similarity between IP_{STN}-HP_{STN} was inversely correlated with the distance between IP_{INPUT}-HP_{GPe}. Each dot represents a pair of IP and HP experiments (n = 55 × 176). Middle: Scatterplots of IP_{STN} and HP_{STN} density from three representative pairs showing similar (1), intermediate (2), and different (3) IP_{STN} and HP_{STN} projections. Right: Prediction of HP_{GPe}-HP_{STN} based on GPe input-IP_{STN} topographic organization resulted in significantly lower mean squared error (MSE) compared with randomizations (***$p < 0.001$, two-sided Student t-test). Red error bars represent the mean with s.e.m, while the gray area represents the 5^{th} to 95^{th} percentile of randomization. **(F)** Left: Injection sites of retroAAV expressing tdTomato and sfGFP in the GPe (top) and STN (bottom), respectively. Right: Magnified image of the MOp showing labeled GPe (red)- and STN (green)-projecting cells in L5, with co-labeled (yellow) cells representing collateral GPe/STN-projecting neurons. Scale bar 1 mm and 100 µm (enlarged view). **(G)** Analysis of single cell reconstruction data from the MouseLight database. Left: representative MOs neuron (AA0772) collaterally

bioRxiv preprint doi: https://doi.org/10.1101/2021.10.01.462690; this version posted October 1, 2021. The copyright holder for this preprint (which was not certified by peer review) is the author/funder, who has granted bioRxiv a license to display the preprint in perpetuity. It is made available under aCC-BY-ND 4.0 International license.

projecting to the GPe and STN. Right: cortical neuronal population innervating the HP_{GPe} (64%), HP_{STN} (20%), and collaterally innervating the $HP_{GPe/STN}$ (15%). **(H)** Schematic illustration of three types of signal integration in the STN from indirect and hyperdirect pathways. Correlations were calculated via Pearson's r.

bioRxiv preprint doi: https://doi.org/10.1101/2021.10.01.462690; this version posted October 1, 2021. The copyright holder for this preprint (which was not certified by peer review) is the author/funder, who has granted bioRxiv a license to display the preprint in perpetuity. It is made available under aCC-BY-ND 4.0 International license.

Figure 4. Glutamatergic STN PV+ neurons. (A) Top: pipeline of serial smFISH data generation and processing. Bottom: example serial smFISH image of STN with the distance from the bregma indicated at the corner. **(B)** Left: example smFISH image of the STN (inset) from coronal brain slice with *Pvalb*, *Slc17a6*, and *Slc32a1*. Right: magnified views of the regions indicated by white boxes in the dorsolateral (top) and ventromedial (bottom) STN (left panel) show that STN neuronal population co-express *Pvalb* and *Slc17a6*, but not *Slc32a1*. Scale bar, 1 mm (left), 250 µm (left, inset), and 10 µm. **(C), (D)** Topographic distribution of glutamatergic PV+ neurons in the STN. Representative smFISH images cropped to show the STN (**C**, left), and quantification of cells expressing each gene along STN axis1 shown with the mean (n = 2) and s.e.m. (**C**, right). The pseudocolor arrow represents STN axis1. Co-expression plot of *Pvalb* with *Slc17a6* (**D**, left) and *Slc32a1* (**D**, right), showing the number of mRNA puncta per cell for each gene. Each dot represents a cell, colored according to location along STN axis1. Dashed lines represent the thresholds for positive cells. Double negative cells are not shown. Scale bar, 250 µm.

bioRxiv preprint doi: https://doi.org/10.1101/2021.10.01.462690; this version posted October 1, 2021. The copyright holder for this preprint (which was not certified by peer review) is the author/funder, who has granted bioRxiv a license to display the preprint in perpetuity. It is made available under aCC-BY-ND 4.0 International license.

Figure 5. Firing patterns of STN PV+/- neuron. (A) Left: representative image of the STN (inset) from coronal brain slice of PV-IRES-Cre::Ai6 mouse line, showing PV+ neurons. Right: magnified immunofluorescence image of STN cells show STN PV+ neurons co-labeled with anti-Glutamate (top) but not with anti-GABA (bottom). Scale bar, 1 mm (left), and 250 µm (left, inset) and 20 µm (right). **(B)** Distribution of PV+ neurons in the STN using automatic cell detection from PV-IRES-Cre::Ai6 mouse. Scale bar, 250 µm. **(C)** Electrophysiological properties of STN PV+/- neurons. Representative tonic (bottom) and burst (top) firing with enlarged traces shown in boxes, recorded from STN PV+/- neurons using the PV-IRES-Cre::Ai6 mouse line. Interspike interval (ISI) of first two, 2^{nd} and 3^{rd}, last two spikes, and average of all spikes shown in the boxes; 7.7, 5.9, 7.7, and 6.5 ms for PV+ burst firing; 50.3, 51.4, 46.7, and 47.5 ms for PV- tonic firing neuron. **(D)** ISI histogram of spontaneous firing patterns (burst PV+ and tonic PV+/- neurons, n = 12, 14, and 20, respectively). Insets in the top panels show magnified ISI histogram during 0-150 ms (shaded area). Bar graph shows the proportion of burst firing cells (right). **(E)** ISI histogram of firing patterns during a rebound depolarization following the removal of a hyperpolarizing current injection (left), and during depolarizing current injection (right; see **Methods**) **(F)** The hyperpolarization-induced depolarizing sag of PV+/- neurons, marked by an arrow (left), was significantly smaller than that in PV+ neurons (right). Data are mean **±** s.e.m. Mann–Whitney U test with $p < 0.01$. ISI of first two, 2^{nd} and 3^{rd}, last two spikes, and average of all spikes; 4.2, 3.5, 8.9, and 4.6 ms for PV+ burst firing, 12.4, 12.5, 55.1, 24.2 ms for PV- tonic firing neuron.

bioRxiv preprint doi: https://doi.org/10.1101/2021.10.01.462690; this version posted October 1, 2021. The copyright holder for this preprint (which was not certified by peer review) is the author/funder, who has granted bioRxiv a license to display the preprint in perpetuity. It is made available under aCC-BY-ND 4.0 International license.

Figure 6. Cell type-dependent synaptic connectivity. (A) Scheme of tested cell type-specific connections in the HP_{GPe} (1, 2), HP_{STN} (3, 4), and IP_{STN} (5, 6). **(B-E)**, Labeling strategies for testing synaptic connections listed in **(A)** using retrograde virus and mGRASP system. Presynaptic-mGRASP was injected into either the cortex (1–4) or the GPe (5–6). Projection-dependent GPe cell types (arkypallidal and prototypic) were labeled with retro-lenti virus expressing Cre in the Striatum and STN, respectively (1, 2), followed by Cre-ON postsynaptic-mGRASP in the GPe. A mixture of postsynaptic-mGRASP and Cre-ON fluorescent protein was injected into the STN of PV-IRES-Cre mice to distinguish STN PV+/- neurons (3–6). **(F)** Post-synaptic neurons (top) and enlarged image of dendrite (bottom), marked by white box. Green mGRASP signals along the dendrites of post-synaptic neurons (red) were detected in all tested sets, indicating the synaptic connections. Scale bar, 10 µm (top), and 2 µm (bottom). **(G)** Representative coronal smFISH image of the STN with *Pvalb*, *Gria1,* and *Gabra1*. Enlarged views of the regions indicated by white boxes in the dorsolateral (top) and ventromedial (bottom) STN (left panel) showing co-expression of *Gria1* and *Gabra1*. Scale bar, 1 mm (left), 250 µm (left, inset) and 20 µm (right). **(H)** Topographic distribution along STN axis1 of cells expressing *Gria1* and *Gabra1*. Quantification of cells expressing each gene along STN axis1 (left) and a co-expression plot (right) showing that most STN cells co-express *Gria1* and *Gabra1*. Data are represented as means (n = 6) with s.e.m. **(I)** Left: Relative expression level of *Gria1* and *Gabra1* in PV+/- neurons. Middle: *Gria1* to *Gabra1* ratio in PV+/- neurons exhibit distinct topographic pattern along STN axis1. Right: the *Gria1* to *Gabra1* ratio was significantly lower in STN PV+ cells (permutation test, n = 10,000, ****$p < 0.0001$). Data are represented as means (n = 6) with s.e.m.

bioRxiv preprint doi: https://doi.org/10.1101/2021.10.01.462690; this version posted October 1, 2021. The copyright holder for this preprint (which was not certified by peer review) is the author/funder, who has granted bioRxiv a license to display the preprint in perpetuity. It is made available under aCC-BY-ND 4.0 International license.

Figure 7. Schematic of basal ganglia network with detailed topographic connectivity, cytoarchitecture, and firing pattern of the STN. (A) Summary of connectivity, cellular and physiological profiles (top) and cell-type specific synaptic connectivity (bottom) of the STN. Topographical organization of three convergent types of indirect and hyperdirect pathways is represented in gradual color change and arrows. Representative traces of two firing patterns, burst and tonic firing, illustrate topographic distribution of functionally distinct cell-types along dorsolateral and ventromedial parts of the STN, respectively. **(B)** Schematic of basal ganglia network with updated circuit- and cellular-level connectivity found in this study (represented in colored line). Three convergent hyperdirect and indirect pathways related to the STN are shown in solid lines.

458

bioRxiv preprint doi: https://doi.org/10.1101/2021.10.01.462690; this version posted October 1, 2021. The copyright holder for this preprint (which was not certified by peer review) is the author/funder, who has granted bioRxiv a license to display the preprint in perpetuity. It is made available under aCC-BY-ND 4.0 International license.

STAR Methods

Mice

C57BL/6J, PV-IRES-Cre (B6;129P2-Pvalb$^{tm1(cre)Arbr}$/J, JAX stock no. 017320), Ai6 (B6.Cg-Gt(ROSA)26Sor$^{tm6(CAG-ZsGreen1)Hze}$/J, JAX stock no. 007906), and double-transgenic PV-IRES-Cre::Ai6 mice were used in this study. While eight 10-week-old mice were used for most experiments, five 7-week-old mice were used for electrophysiology. All experiments were conducted in accordance with protocols approved by the Institutional Animal Care and Use Committee at the Korea Institute of Science and Technology and the National Institutes of Health guidelines for animal care and use.

Stereotaxic injection

Iontophoresis of recombinant adeno-associated virus (rAAV) vectors was performed by applying a positive current for 5 min using a Digital Midgard Precision Current Source (Stoelting). For indirect pathway mapping experiments, rAAV2/1.CAG.sfGFP.WPRE or rAAV2/1.CAG.tdTomato.WPRE (average titer from seven batches: 1.7 x 10^{13} vg/ml) was injected via a 3 μA current into the GPe. Unilateral dual-injections were performed in 35 mice with a total of 55 injections (**Table S1**). For HP_{STN} labeling, retroAAV-expressing iCre, rAAV2.CAG.iCre.WPRE packaged with a rAAV2-retro helper (Addgene, 51904 and 81070)(Kato et al., 2014; Tervo et al., 2016), was injected via a 5 μA current into the STN of Ai6 mice. For other surgeries, pressure injections were performed at 20–40 nl per min using a Nanoliter injector and a Micro-4 syringe pump (World Precision Instruments). For cortico-pallidal pathway labeling, rAAV2/retro.CAG.iCre.WPRE and rAAV2/1.CAG.JxON.tdTomato.WPRE (100 nl each) were injected into the GPe and ipsilateral primary motor cortex (MOp). For cortico-pallidal pathway dissection, rAAV2/retro.CAG.sfGFP.WPRE and rAAV2/retro.CAG.tdTomato.WPRE (100 nl each) were injected into the STN and the GPe, respectively. For synaptic connectivity mapping, improved mGRASP (Kim et al., 2012) combined with a retro-Lenti system (Kato et al., 2014) or

bioRxiv preprint doi: https://doi.org/10.1101/2021.10.01.462690; this version posted October 1, 2021. The copyright holder for this preprint (which was not certified by peer review) is the author/funder, who has granted bioRxiv a license to display the preprint in perpetuity. It is made available under aCC-BY-ND 4.0 International license.

transgenic mouse line was used. For mapping cell type-specific synaptic connectivity, pre- and post-synaptic mGRASP components were injected into the cortex/GPe and STN. mGRASP technology has been demonstrated to be an accurate synaptic detector and has been successfully employed in the mapping of fine-scale synaptic connectivity in multiple cell types in various circuits (Druckmann et al., 2014; Feng et al., 2014; Kim et al., 2012; Kwon et al., 2018; Mukherjee et al., 2020; Song et al., 2018). To validate synaptic connections in hyper-/indirect pathways using mGRASP, rAAV2/1.CAG.pre-mGRASPi.OLLAS.WPRE was injected into the MOp (600 nl) or GPe (400 nl), respectively. For post-mGRASP labeling specific to GPe cell types, 50 nl of retroLenti/FuG-E.CAG.iCre.WPRE was injected into the striatum or STN, and 100 nl of rAAV2/1.CAG.JxON.post-mGRASP.2A.dTomato.WPRE (Addgene, 34913) was injected into the GPe. For post-mGRASP labeling specific to STN cell types, a mixture of rAAV2/1.CAG.post-mGRASP.2A.dTomato.WPRE (Addgene, 34912) and rAAV2/1.CAG.JxON.iRFP670.WPRE (4:1 ratio) was injected into the STN of PV-IRES-Cre mice (50 nl). The following coordinates (in mm) were used for the GPe: -0.22 anterioposterior from bregma (AP), +2.0 mediolateral from bregma (ML), -3.5 dorsoventral from dura (DV); STN: -1.65 AP, +1.6 ML, -4.55 or -4.65 DV (for PV-IRES-Cre); MOp: +2.0 AP, +1.75, +2.0, and +2.25 ML, -0.8 and -0.9 DV; and striatum: +0.5 AP, +2.0 ML, -3.0, -2.5, and -2.0 DV. The viral vectors were packaged using vector cores at the University of Pennsylvania or the University of North Carolina at Chapel Hill.

Tissue preparation

Brains were prepared as previously described(Feng et al., 2014). For GABA immunofluorescence, 4% paraformaldehyde in 0.1M phosphate buffer with pH 7.4 (4% PFA) containing 0.3% glutaraldehyde was used for fixation. For immunofluorescence, 50-μm sections were permeabilized in 1% Trition X-100 in tris-buffered saline (TBS) and blocked in 5% normal goat serum and 0.4% Trition X-100 in TBS. The sections were incubated with primary antibody for 1–2 days at 4 ºC. After washing, the sections were incubated with secondary antibody for 2–3 h at room temperature and counterstained with DAPI, except for in the mGRASP experiments.

bioRxiv preprint doi: https://doi.org/10.1101/2021.10.01.462690; this version posted October 1, 2021. The copyright holder for this preprint (which was not certified by peer review) is the author/funder, who has granted bioRxiv a license to display the preprint in perpetuity. It is made available under aCC-BY-ND 4.0 International license.

Sections were mounted with mounting media (Invitrogen, Prolong Diamond Antifade or Vector Labs, VectaShield). In this study, we used the following antibodies: rat anti-OLLAS (Novus, NBP1-06713, 1:1000), guinea pig anti-NeuN (Sigma-Aldrich, ABN90P, 1:1000), rabbit anti-glutamate (Sigma-Aldrich, G6642, 1:500-1000), rabbit anti-GABA (Sigma-Aldrich, A2052, 1:500-1000), Alexa Fluor 488 goat anti-rabbit IgG (Invitrogen, A11008, 1:200), Alexa Fluor 555 goat anti-guinea pig IgG (Invitrogen, A21435, 1:200), Alexa Fluor 633 goat anti-rabbit IgG (Invitrogen, A21071, 1:500), and Alexa Fluor 633 goat anti-rat IgG (Invitrogen, A21094, 1:1000).

For tissue clearing, we modified the CLARITY method (Tomer et al., 2014). Briefly, PFA-fixed brains were cut as parasagittal sections (2.5 mm) containing the GPe and STN. The sections were incubated for at least 2 days in a hydrogel solution with the following composition (in %): 1 acrylamide, 4 PFA, and 0.25 VA-044 initiator in PBS. Following degassing and gel polymerization at 37 ºC, the sections were incubated in SmartClear Clearing Buffer Type A (LifeCanvas Technologies) at 37 ºC and in EasyIndex (LifeCanvas Technologies) at room temperature.

Microscopy

Wide-field images were obtained using an Axioscan Z1 slide scanner (Carl Zeiss Microscopy) equipped with a 20X 0.8 NA Plan-Apochromat air lens. Confocal images were acquired using an LSM 780 confocal microscope (Carl Zeiss Microscopy). mGRASP images were obtained at 0.6 µm depth intervals using a 40x 1.4 NA Plan Apochromat oil lens with a 2-fold digital zoom. For cleared tissue imaging, each sample was mounted with EasyIndex. Cleared brain images were acquired at 8.0 µm depth intervals using a 20x 1.0 NA Plan-Neofluar optimized for CLARITY (Carl Zeiss Microscopy). Single-molecule fluorescence *in situ* hybridization (smFISH) images were acquired at 1 or 2 µm depth intervals using a 40x 1.3 NA oil immersion lens.

Indirect projection mapping pipeline

bioRxiv preprint doi: https://doi.org/10.1101/2021.10.01.462690; this version posted October 1, 2021. The copyright holder for this preprint (which was not certified by peer review) is the author/funder, who has granted bioRxiv a license to display the preprint in perpetuity. It is made available under aCC-BY-ND 4.0 International license.

The MATLAB (https://www.mathworks.com) version of the BaSiC (Peng et al., 2017) algorithm was applied to each fluorescent channel of image tiles (2040 px x 2040 px) using the default parameters for shading correction. Using a custom built GUI, image series were manually inspected for 1) missing or damaged tissue and 2) mispositioning, including flipping and rotation. Image series with severe artifacts in either the GPe or STN were consequently removed from the study. Human experts manually annotated the locations of the injection sites to encompass the cell bodies of labeled neurons, and a morphological operation was performed to generate a smooth binary injection mask. The injection volume of the filtered dataset (n = 55) averaged 0.1403 ± 0.0797 mm^3 (0.0546 ± 0.031 mm^3 within the GPe).

The custom signal detection algorithm was applied to each image to extract positive signals from the background autofluorescence. The autofluorescence distribution of each image series was estimated from the non-signal regions contralateral to the injection site, and the mean was subsequently subtracted from the image. A median filter (3 x 3) was applied to reduce the noise. Candidate signal objects were first detected using the autofluorescence intensity profile and classified into three groups based on the intensity. Low- and medium-intensity objects were combined with the detection result from the edge detection filter (k_{width} = 10, 30). The binary signal masks generated from the detection results were used to classify each pixel as either signal or background, and the density within a 10 μm × 10 μm grid was computed.

Images were first pre-aligned sequentially to minimize the inter-sectional difference in the DAPI signal. Stacked image volumes were aligned to the Allen Common Coordinate Framework (CCF v3) (Wang et al., 2020) via iterative 3D global and two-dimensional (2D) slice affine alignment using elastix (Klein et al., 2010). A population average model from 35 aligned volumes was generated following the Allen informatics data pipeline (Kuan et al., 2015), then registered to the CCF v3 using the Symmetric Normalization (SyN) transformation model (Avants et al., 2008) from Advanced Neuroimaging Tools (ANTs, https://github.com/ANTsX/ANTs). 3D deformable transformation from the population-averaged model to the CCF v3 was applied to each DAPI-based volume and the corresponding signal image was used to generate a 25 μm isotropic 3D

bioRxiv preprint doi: https://doi.org/10.1101/2021.10.01.462690; this version posted October 1, 2021. The copyright holder for this preprint (which was not certified by peer review) is the author/funder, who has granted bioRxiv a license to display the preprint in perpetuity. It is made available under aCC-BY-ND 4.0 International license.

registered volume. Injection and projection density signals within the GPe and STN were segmented using 3D region annotation from the Allen Mouse Brain Atlas and stored in a vectorized form. Signals in the GPe were downsampled to an isotropic voxel-size of 50 µm to facilitate computation. Signal volumes were computed as the sum of the signal density within the target structure, multiplied by the voxel size.

To limit false positive projection signals, image series with (1) low injection or projection volume (< 0.001 mm^3) or (2) ectopic injections at the central nucleus of the amygdala (CeA) or substantia innominata (SI) were removed.

Hyperdirect projection data from the AMBCA

Using the API for the Allen Mouse Brain Connectivity Atlas (AMBCA, https://connectivity.brain-map.org), we downloaded the dataset of isocortical injections with GPe or STN projections (n_{gpe} = 1270, n_{stn} = 851, at the time of our analysis). The voxel resolution for isotropic volume was set to 50 µm for injections and the GPe projection density, and 25 µm for the STN projection density. Injection sites were inspected to remove experiments in which more than 10% of the injection volume was located outside the isocortex. The minimum projection volume for both the GPe and STN was set to 0.001 mm^3. We included nine transgenic Cre-lines with at least five datasets (Table S3) in addition to a dataset for wild-type C57BL/6J, which result in 176 datasets in total (181 for HP_{STN}).

Trainable WEKA Segmentation (http://fiji.sc/Trainable_Weka_Segmentation) plugin for Fiji was used to identify and subtract passing fibers in the GPe and STN. The WEKA Segmentation model was trained using set of manually annotated labeled images containing labels for 1) densely populated thick fasciculated axon fibers, 2) fine axon projections, and 3) background. Among 86 datasets with densely populated projection signal (density > 0.5) in GPe, 25% were randomly selected for training dataset (n_{train} = 22). Selection of filters and parameters were same as described in Hunnicutt *et al*(Hunnicutt et al., 2016). After training, the classifier was applied to remaining dataset and generated a probability map for each label. To minimize the

bioRxiv preprint doi: https://doi.org/10.1101/2021.10.01.462690; this version posted October 1, 2021. The copyright holder for this preprint (which was not certified by peer review) is the author/funder, who has granted bioRxiv a license to display the preprint in perpetuity. It is made available under aCC-BY-ND 4.0 International license.

593 artifacts from thick fasciculate fibers, conservative segmentation criteria was set to subtract as
594 much passing fiber signal as possible. Default classification threshold was set to $P_{fiber} > 0.25$ for
595 fasciculated fiber, and $P_{signal} > 0.7$ for axon signal classification. Custom built GUI in MATLAB was
596 used to inspect the classification result, and to manually tune the segmentation threshold for each
597 data if needed.
598
599 **Single-neuron reconstruction data from the MouseLight database**
600 Single neuron reconstruction data were obtained from the MouseLight database using Neuron
601 Browser (http://www.mouselight.janelia.org). The search query was set to include only neurons
602 for which the soma was located within the isocortex and any axonal structures were in either the
603 GPe or STN (**Figure S5B**), which resulted in 142 reconstructed neurons. Neurons whose soma
604 was located in the left hemisphere were mirrored onto the right hemisphere. Reconstructed
605 neurons without ipsi-lateral projections to the GPe or STN were removed, and the remaining
606 neurons (n = 69) were classified by projection pattern: (1) IT types showing contralateral
607 projections (n = 24/69); (2) Collateral $HP_{STN/GPe}$ (n = 10/69); (3) HP_{STN} only (n = 15/69); and (4)
608 HP_{GPe} only (n = 20/69).
609 Normalized projection density was computed as the length of axons within the region
610 normalized by the region volume. To visualize the topographical organization (Figure S5D), only
611 neurons with axonal projections longer than 100 μm in both the GPe and STN were shown.
612
613 **Analysis of mouse hyper/indirect pathway topographic organization**
614 The projection centroid was defined as the weighted centroid of the 3D density signal within a
615 target region. The distance between two projections was measured using the pairwise cosine
616 distance between two vectorized projections. STN geometric axis1 and axis2 were defined as the
617 principal axis and its perpendicular, respectively, in a 2D projection of the STN along the AP axis.
618 For the signal distribution heatmap, reconstructed signals were digitally resliced along a
619 designated axis and the fraction of signal volume within each slice to the total signal volume was

bioRxiv preprint doi: https://doi.org/10.1101/2021.10.01.462690; this version posted October 1, 2021. The copyright holder for this preprint (which was not certified by peer review) is the author/funder, who has granted bioRxiv a license to display the preprint in perpetuity. It is made available under aCC-BY-ND 4.0 International license.

computed. The similarities between signal distributions were measured using the Pearson correlation between the signal centroid location along each direction.

We applied classical multi-dimensional scaling (MDS) (Kruskal and Wish, 1978) to visualize the pairwise projection distance relationships between STN projections in the "pattern space". Robust Canonical Correlation Analysis (rCCA) (Branco et al., 2005) was performed to identify the graded topographic organization between the locations of each projection in the pattern space and the injection centroid in the anatomical space. MDS embeddings were then rotated so that the major axes corresponded to the canonical variates. Gradient axes in the cortex and the GPe corresponding to the STN geometric axes were computed via ridge regression on the STN projection centroid location along the gradient axis and input centroid coordinates.

Injections for which the majority (> 80%) of the injection volume was contained within the primary injection structure were classified as localized injections and used to investigate projection patterns from a single cortical subregion. Projection density signals from localized injections into the target structure were rescaled to [0, 1], then averaged to generate a characteristic projection. Note that the resulting characteristic projection may reflect only the spatial pattern of the projection, and its intensity may not be comparable to characteristic projections from other regions.

The projection power of a functional subregion, which represents an estimated projection volume assuming the subregion is fully labeled, was computed using non-negative ridge regression on the projection volume with the vector containing the injection volume within each subregion normalized by its volume, as a regressor.

The topographic relationship between IP_{STN}-IP_{INPUT} was modeled using a multivariate linear model with the IP_{STN} centroid locations along two gradient axes as observations and the IP_{INPUT} injection centroids as predictors. The same model was assessed using HP_{STN} centroids as inputs and HP_{GPe} centroids as targets. Error was measured according to the distance between the actual and predicted HP_{GPe} centroids. Permutation tests were used to compare the means of observed error against the error from 10,000 randomizations, where for each HP_{STN}, the

bioRxiv preprint doi: https://doi.org/10.1101/2021.10.01.462690; this version posted October 1, 2021. The copyright holder for this preprint (which was not certified by peer review) is the author/funder, who has granted bioRxiv a license to display the preprint in perpetuity. It is made available under aCC-BY-ND 4.0 International license.

corresponding HP_{GPe} was reassigned by shuffling. Two-sided t-tests were used to compare the means of the two groups.

In addition, to test whether nearby cortical injections targeting different functional subregions resulted in clearly segregated STN projection patterns, we measured the STN projection pattern distances between pairs of experiments using the following criteria: 1) the two injection volumes are localized within different functional tripartite cortical subregions; 2) the injection volumes exhibit no overlap in the reference space; 3) the distance between injection centroids is greater than 1 mm and less than 1.5 mm. We compared the distribution and mean of the STN projection distances from pairs of nearby injections targeting different subregions and pairs with the same input subregion using two-sided t-tests.

Serial Single-Molecule Fluorescence In Situ Hybridization

Mouse brains were collected and immediately frozen in -80 ºC 100% ethanol. Coronal sections (20 µm) containing the STN were collected using a cryostat (Leica) and mounted on SuperFrost microscope slides (FisherBrand). Serial smFISH was performed using the RNAscope multiplex fluorescent kit (ACD bio, 320850) according to the manufacturer's protocols. Brain sections were fixed in 4% PFA and dehydrated serially in ethanol (50%, 70%, 100%, and 100%). Sections were incubated in proteinase IV and rinsed with PBS. Probes were applied for 2 h at 40 ºC and amplifiers 1–4 were subsequently applied at 40 ºC. We used probes for *Aqp4* (catalog no. 417161), *Gabra1* (435451), *Gria1* (421931), *Mbp* (451491), *Pvalb* (421931), *Rbfox3* (313311), *Slc17a6* (319171), *Slc32a1* (319191), and *Tmem119* (472901). Sections were counterstained with DAPI.

A nucleus detection pipeline, as previously described (Feng et al., 2019), was trained on 30 images containing DAPI-stained cell nuclei (~180 per image) that were manually labeled by human experts. To detect mRNA puncta, we used a splitting strategy with a marker-controlled watershed approach and a variational Bayesian Gaussian mixture model (Feng et al., 2012). The

bioRxiv preprint doi: https://doi.org/10.1101/2021.10.01.462690; this version posted October 1, 2021. The copyright holder for this preprint (which was not certified by peer review) is the author/funder, who has granted bioRxiv a license to display the preprint in perpetuity. It is made available under aCC-BY-ND 4.0 International license.

673 detected mRNA puncta were assigned to the nearest detected nuclei with a maximum distance of
674 1 μm.

675 Human experts manually registered each smFISH image section to a corresponding slice
676 in Allen CCF v3, using a GUI that was custom designed in MATLAB, via rigid transformation
677 (reflections, translation, and rotations). Support Vector Machine was then used to determine the
678 threshold for positive cell classification. A classification model was trained on 30 randomly
679 selected and manually labeled cells per image section, using the number, size, and intensity of
680 puncta as the input.

681

682 **Electrophysiological recording**

683 Mice were anesthetized with halothane and transcardially perfused with an ice-cold dissection
684 solution containing (in mM): 228 Sucrose, 2.5 KCl, 7 $MgSO_4$, 0.5 $CaCl_2$, 1.25 NaH_2PO_4, 26
685 $NaHCO_3$, and 11 glucose, oxygenated with 95% O_2 and 5% CO_2. The brains were quickly
686 removed and parasagittal slices (250 μm) containing the STN were prepared using a vibratome
687 (Leica VT 1200S) in cold dissection solution. Slices were then transferred into extracellular
688 solution containing (in mM): 125 NaCl, 2.5 KCl, 1.3 $MgSO_4$, 2.5 $CaCl_2$, 1.25 NaH_2PO_4, 26
689 $NaHCO_3$, and 11 glucose, oxygenated with 95% O_2 and 5% CO_2, in which they were constantly
690 kept before being moved to the recording chamber which also contained the extracellular
691 solution. Chemicals for electrophysiological analyses were obtained from Sigma or Wako Pure
692 Chemical Industries unless otherwise specified.

693 Whole-cell patch clamp recordings were made from ZsGreen-positive or ZsGreen-
694 negative neurons in the STN of PV-IRES-Cre::Ai6 mice. Patch pipettes (resistance 5-6 MΩ) were
695 filled with a solution containing (in mM): 130 potassium gluconate, 2 NaCl, 4 $MgCl_2$, 4 Na_2ATP,
696 0.4 NaGTP, 20 HEPES (pH 7.2), and 0.25 EGTA. Recordings in the cell-attached configuration
697 were sometimes conducted before making whole-cell recordings. Neurons in the STN were
698 visualized directly using a BX61WI microscope (Olympus), and those expressing ZsGreen were
699 identified by a FV1000 confocal microscope (Olympus). Membrane potentials were recorded in

bioRxiv preprint doi: https://doi.org/10.1101/2021.10.01.462690; this version posted October 1, 2021. The copyright holder for this preprint (which was not certified by peer review) is the author/funder, who has granted bioRxiv a license to display the preprint in perpetuity. It is made available under aCC-BY-ND 4.0 International license.

current-clamp mode either without current injection, or by giving depolarizing (100 pA) or hyperpolarizing (-200 pA) current steps for 500 ms, using a Multiclamp 700B amplifier and pClamp software (Molecular Devices). Data were accepted if the input membrane resistance was > 100 MΩ, firing action potentials had an amplitude of at least 50 mV, and the afterhyperpolarizing potential was < -50 mV. Analyses of electrophysiological parameters were performed using OriginPro (https://www.originlab.com) and Clampex (https://www.moleculardevices.com) software. The peak of afterhyperpolarizing potential was considered as membrane potential during firing. The parameter values for action potentials were equivalent to a previous study (Beurrier et al., 1999). Statistical significance was evaluated using the Mann-Whitney U test. In this study, to examine two neuronal firing patterns (tonic and burst firing), we classified burst firing according to the presence of, at least, one of the following firing patterns in three sequential recording conditions: 1) When recording without current injection, spontaneous firing shows fast burst firing (< 10 ms inter-spike intervals, ISI, on average) followed by a pause. Similar to the previously reported burst firing in the STN (Beurrier et al., 1999; Huang et al., 2017; Kass and Mintz, 2006), the membrane potential tends to be depolarized during burst firing, and tends to be drastically hyperpolarized at the start of a pause; 2) when recording during a 250-ms period of rebound depolarization following the removal of a hyperpolarizing current injection (-200 pA), the firing frequency is fast (< 10 ms ISI on average) and the membrane potential tends towards depolarization, followed by drastic hyperpolarization (> 15 pA) and quiescence of firing; 3) when recording during a 500-ms depolarizing current injection (100 pA), the firing frequency is fast (< 10 ms ISI on average) and the membrane potential tends towards depolarization at the beginning of a depolarizing current injection, followed by quiescence of firing for more than 50 ms (e.g., the top-right trace in **Figure S9C**). The firing properties used for this classification were compared between burst PV+, tonic PV+, and tonic PV- neurons. We noted that the properties of burst firing neurons generally differed from those of tonic firing neurons and that there was a clear tendency for firing to slow down during bursts, as reflected by the significant difference between the first or second ISI and the last ISI.

bioRxiv preprint doi: https://doi.org/10.1101/2021.10.01.462690; this version posted October 1, 2021. The copyright holder for this preprint (which was not certified by peer review) is the author/funder, who has granted bioRxiv a license to display the preprint in perpetuity. It is made available under aCC-BY-ND 4.0 International license.

Human 7T-DTI tractography

T2*-weighted imaging (T2*WI) with 0.2 mm in-plane resolution and diffusion-weighted imaging (DWI) along 64 directions with a b-value of 2000 s/mm^2 and b0 with 1.8 mm isotropic resolution were obtained from a healthy 30-year-old adult male using a 7.0T MRI scanner (Magnetom, Siemens) and a homemade 8-channel radiofrequency head coil (Gachon University) (Cho et al., 2014). A 3D T1-weighted whole brain scan was obtained for anatomical reference using a 3.0T MRI scanner (Magnetom Verio, Siemens).

The DWI data were preprocessed to correct geometric distortions (Oh et al., 2012). Axonal fiber orientation information was calculated using a constrained spherical deconvolution-based diffusion model in the MRtrix3 toolbox (https://www.mrtrix.org)(Tournier et al., 2010). Whole-brain streamline tractography was performed using the probabilistic algorithm, iFOD1, as implemented in the MRtrix3 and visualized by track-density imaging (TDI) (Calamante et al., 2010) with a 0.2 mm isotropic resolution. Stacked T2*-WIs were interpolated to an isotropic 0.2 mm resolution and then co-registered to the b0 volume image of the DWI data using SPM12 (https://www.fil.ion.ucl.ac.uk/spm/software). The regions-of-interest, including the STN and GPe, were manually traced using the MRtrix3, and the 3D Slicer (http://www.slicer.org) was used for 3D modeling. T1-images were registered to the b0 volume image of DWI scans via affine transformation and annotated using the human Brainnetome atlas (Fan et al., 2016), mapped using FreeSurfer (http://surfer.nmr.mgh.harvard.edu).

Probabilistic constrained spherical deconvolution-based fiber tracking was performed using the iFOD2 algorithm (Oh et al., 2012). Optimal parameters were determined such that the resulting streamlines were visually similar to the combined subset of streamlines filtered according to anatomical constraints (Desmond et al., 1995). An additional five parameter combinations with values close to the selected parameters were also used. Whole-track and end-point TDI maps were computed using tracks that terminated within the STN.

bioRxiv preprint doi: https://doi.org/10.1101/2021.10.01.462690; this version posted October 1, 2021. The copyright holder for this preprint (which was not certified by peer review) is the author/funder, who has granted bioRxiv a license to display the preprint in perpetuity. It is made available under aCC-BY-ND 4.0 International license.

The normalized average density of tracks in a region was defined as the average track intensity of all voxels within the TDI map of the target subregion. The spatial overlap was defined as $\frac{\sum_{|A\cap B|} min(A_i,B_j)}{\sum_{|A\cup B|} max(A_i,B_j)}$, where A_i and B_j are the voxel intensities from two subregions.

Human deep brain stimulation

This study included 26 patients who received bilateral STN DBS implantation between March 2005 and December 2008 at the Movement Disorder Center of Seoul National University Hospital (SNUH). The criteria were electrical stimulation of the left STN with a mono-polar electrode configuration and follow-up period of more than 3 years.

Pre-operative MRI images were obtained using a 1.5 T Signa MRI system (General Electric Medical Systems). STN DBS implantation was performed using a Leksell frame and SurgiPlan with microelectrode recording and macro-stimulation under local anesthesia, as previously described (Kim et al., 2009, 2010). The dorsolateral portion of the STN was targeted using MRI images, with theoretical STN coordinates (4 mm anterior from the midcommissural point, 10–12 mm lateral from the midline, and 3–4 mm below the intercommissural line). Permanent DBS electrode (Medtronic, DBS 3389) placement was determined to avoid damage to adjacent vessels, ventricles, and sulci.

Three-dimensional spiral stereotactic CT scans (Philips, Brilliance CT 64-channel) with 1 mm thick slices were taken more than 1 month after surgery as previously described(Paek et al., 2008). The post-operative CT images were co-registered to pre-operative MRI images that were normalized to the ICBM 152 2009b nonlinear asymmetric T2 template (Fonov et al., 2011). The electrode trajectories were pre-reconstructed from post-operative CT images and manually adjusted. All normalization and registration processes were done using Lead-DBS (Horn and Kühn, 2015). Electrode trajectories were plotted onto images from the Schaltenbrand and Wahren human brain atlas for 2D visualization (Schaltenbrand and Wahren, 1998).

bioRxiv preprint doi: https://doi.org/10.1101/2021.10.01.462690; this version posted October 1, 2021. The copyright holder for this preprint (which was not certified by peer review) is the author/funder, who has granted bioRxiv a license to display the preprint in perpetuity. It is made available under aCC-BY-ND 4.0 International license.

Neurologists evaluated the patients using the Unified Parkinson Disease Rating Scale (UPDRS) before and at 12, 24, 36, and 60 (if applicable) months after surgery. Motor symptom improvement was measured as a post-operative change in the summed UPDRS motor score (UPDRS III) of the right limb.

Data Availability

The datasets generated and analyzed supporting the findings of this study are available from the corresponding author upon reasonable request.

Code availability

Custom code used in this study are available from the corresponding author upon request.

Supplemental Information

9 Figures; **6** Tables; **2** Movies

Data	Title	Related to
Figure. S1	Mesoscale connectivity data processing pipeline	Figure 1
Figure. S2	Overview of individual indirect pathway dataset	Figure 1
Figure. S3	Graded topographic organization of indirect pathway	Figure 1
Figure. S4	Characteristics of hyperdirect pathway dataset	Figure 2
Figure. S5	Topographic organization of hyperdirect pathway	Figure 3
Figure. S6	Topographic analysis of human hyperdirect pathway using 7T-MRI	Figure 3
Figure. S7	Cellular composition of the STN by serial-smFISH	Figure 4
Figure. S8	Electrophysiological properties of STN PV+ neurons	Figure 5
Figure. S9	Electrode position-dependent therapeutical effects in clinical DBS trials	Main text
Table S1	GPe injection summary	Figure 1
Table S2	Abbreviations	Figure 2
Table S3	List of transgenic Cre-lines used for hyperdirect pathway	Figure 2
Table S4	7T-MRI parameters	Figure 3
Table S5	Electrophysiological parameters of STN PV+/- neurons	Figure 5

bioRxiv preprint doi: https://doi.org/10.1101/2021.10.01.462690; this version posted October 1, 2021. The copyright holder for this preprint (which was not certified by peer review) is the author/funder, who has granted bioRxiv a license to display the preprint in perpetuity. It is made available under aCC-BY-ND 4.0 International license.

Table S6	Firing properties of burst and tonic firing neurons	Figure 5
Movie S1	Aligned and registered 3D reconstructed whole brain slices using optimized mesoscopic mapping pipeline	Figure 1
Movie S2	High resolution imaging and reconstruction of cleared STN of PV-IRES-Cre::Ai6 mice	Figure 5

794

bioRxiv preprint doi: https://doi.org/10.1101/2021.10.01.462690; this version posted October 1, 2021. The copyright holder for this preprint (which was not certified by peer review) is the author/funder, who has granted bioRxiv a license to display the preprint in perpetuity. It is made available under aCC-BY-ND 4.0 International license.

References

795 Abecassis, Z.A., Berceau, B.L., Win, P.H., García, D., Xenias, H.S., Cui, Q., Pamukcu, A.,
796 Cherian, S., Hernández, V.M., Chon, U., et al. (2020). Npas1+-Nkx2.1+ Neurons Are an Integral
797 Part of the Cortico-pallido-cortical Loop. J Neurosci *40*, 743–768.

798 Alkemade, A., and Forstmann, B.U. (2014). Do we need to revise the tripartite subdivision
799 hypothesis of the human subthalamic nucleus (STN)? Neuroimage *95*, 326–329.

800 Alkemade, A., Hollander, G. de, Miletic, S., Keuken, M.C., Balesar, R., Boer, O. de, Swaab, D.F.,
801 and Forstmann, B.U. (2019). The functional microscopic neuroanatomy of the human subthalamic
802 nucleus. Brain Struct Funct *224*, 3213–3227.

803 Avants, B.B., Epstein, C.L., Grossman, M., and Gee, J.C. (2008). Symmetric diffeomorphic image
804 registration with cross-correlation: Evaluating automated labeling of elderly and
805 neurodegenerative brain. Med Image Anal *12*, 26–41.

806 Benabid, A.L., Chabardes, S., Mitrofanis, J., and Pollak, P. (2009). Deep brain stimulation of the
807 subthalamic nucleus for the treatment of Parkinson's disease. Lancet Neurology *8*, 67–81.

808 Bergman, H., Wichmann, T., and DeLong, M. (1990). Reversal of experimental parkinsonism by
809 lesions of the subthalamic nucleus. Science *249*, 1436–1438.

810 Beurrier, C., Congar, P., Bioulac, B., and Hammond, C. (1999). Subthalamic Nucleus Neurons
811 Switch from Single-Spike Activity to Burst-Firing Mode. J Neurosci *19*, 599–609.

812 Bevan, M.D. (2017). Chapter 14 The Subthalamic Nucleus. Handb Behav Neurosci *24*, 277–291.

813 Branco, J.A., Croux, C., Filzmoser, P., and Oliveira, M.R. (2005). Robust canonical correlations:
814 A comparative study. Computation Stat *20*, 203–229.

815 Calamante, F., Tournier, J.-D., Jackson, G.D., and Connelly, A. (2010). Track-density imaging
816 (TDI): Super-resolution white matter imaging using whole-brain track-density mapping.
817 Neuroimage *53*, 1233–1243.

818 Cho, Z.-H., Calamante, F., and Chi, and J.-G. (2014). 7.0 Tesla MRI Brain White Matter Atlas
819 (Springer).

820 Chu, H.-Y., McIver, E.L., Kovaleski, R.F., Atherton, J.F., and Bevan, M.D. (2017). Loss of
821 Hyperdirect Pathway Cortico-Subthalamic Inputs Following Degeneration of Midbrain Dopamine
822 Neurons. Neuron *95*, 1306-1318.e5.

823 Cobos, I., Calcagnotto, M.E., Vilaythong, A.J., Thwin, M.T., Noebels, J.L., Baraban, S.C., and
824 Rubenstein, J.L.R. (2005). Mice lacking Dlx1 show subtype-specific loss of interneurons, reduced
825 inhibition and epilepsy. Nat Neurosci *8*, 1059–1068.

826 DeLong, M.R., and Wichmann, T. (2015). Basal Ganglia Circuits as Targets for Neuromodulation
827 in Parkinson Disease. Jama Neurol *72*, 1354–1360.

828 del Pino, I., García-Frigola, C., Dehorter, N., Brotons-Mas, J.R., Alvarez-Salvado, E.,
829 Martínez de Lagrán, M., Ciceri, G., Gabaldón, M.V., Moratal, D., Dierssen, M., et al. (2013).

bioRxiv preprint doi: https://doi.org/10.1101/2021.10.01.462690; this version posted October 1, 2021. The copyright holder for this preprint (which was not certified by peer review) is the author/funder, who has granted bioRxiv a license to display the preprint in perpetuity. It is made available under aCC-BY-ND 4.0 International license.

Erbb4 Deletion from Fast-Spiking Interneurons Causes Schizophrenia-like Phenotypes. Neuron *79*, 1152–1168.

Desmond, J.E., Sum, J.M., Wagner, A.D., Demb, J.B., Shear, P.K., Glover, G.H., Gabrieli, J.D.E., and Morrell, M.J. (1995). Functional MRI measurement of language Lateralization in Wada-tested patients. Brain *118*, 1411–1419.

Draganski, B., Kherif, F., Klöppel, S., Cook, P.A., Alexander, D.C., Parker, G.J.M., Deichmann, R., Ashburner, J., and Frackowiak, R.S.J. (2008). Evidence for Segregated and Integrative Connectivity Patterns in the Human Basal Ganglia. J Neurosci *28*, 7143–7152.

Druckmann, S., Feng, L., Lee, B., Yook, C., Zhao, T., Magee, J.C., and Kim, J. (2014). Structured Synaptic Connectivity between Hippocampal Regions. Neuron *81*, 629–640.

Eisenstein, S.A., Koller, J.M., Black, K.D., Campbell, M.C., Lugar, H.M., Ushe, M., Tabbal, S.D., Karimi, M., Hershey, T., Perlmutter, J.S., et al. (2014). Functional anatomy of subthalamic nucleus stimulation in Parkinson disease. Ann Neurol *76*, 279–295.

Fan, K.Y., Baufreton, J., Surmeier, D.J., Chan, C.S., and Bevan, M.D. (2012). Proliferation of External Globus Pallidus-Subthalamic Nucleus Synapses following Degeneration of Midbrain Dopamine Neurons. J Neurosci *32*, 13718–13728.

Fan, L., Li, H., Zhuo, J., Zhang, Y., Wang, J., Chen, L., Yang, Z., Chu, C., Xie, S., Laird, A.R., et al. (2016). The Human Brainnetome Atlas: A New Brain Atlas Based on Connectional Architecture. Cereb Cortex *26*, 3508–3526.

Feng, L., Zhao, T., and Kim, J. (2012). Improved synapse detection for mGRASP-assisted brain connectivity mapping. Bioinformatics *28*, i25–i31.

Feng, L., Kwon, O., Lee, B., Oh, W.C., and Kim, J. (2014). Using mammalian GFP reconstitution across synaptic partners (mGRASP) to map synaptic connectivity in the mouse brain. Nat Protoc *9*, 2425–2437.

Feng, L., Song, J.H., Kim, J., Jeong, S., Park, J.S., and Kim, J. (2019). Robust Nucleus Detection With Partially Labeled Exemplars. Ieee Access *7*, 162169–162178.

Fonov, V., Evans, A.C., Botteron, K., Almli, C.R., McKinstry, R.C., Collins, D.L., and Group, the B.D.C. (2011). Unbiased average age-appropriate atlases for pediatric studies. Neuroimage *54*, 313–327.

Gradinaru, V., Mogri, M., Thompson, K.R., Henderson, J.M., and Deisseroth, K. (2009). Optical Deconstruction of Parkinsonian Neural Circuitry. Science *324*, 354–359.

Group, D.-B.S. for P.D.S. (2001). Deep-Brain Stimulation of the Subthalamic Nucleus or the Pars Interna of the Globus Pallidus in Parkinson's Disease. New Engl J Medicine *345*, 956–963.

Harris, J.A., Mihalas, S., Hirokawa, K.E., Whitesell, J.D., Choi, H., Bernard, A., Bohn, P., Caldejon, S., Casal, L., Cho, A., et al. (2019). Hierarchical organization of cortical and thalamic connectivity. Nature *575*, 195–202.

bioRxiv preprint doi: https://doi.org/10.1101/2021.10.01.462690; this version posted October 1, 2021. The copyright holder for this preprint (which was not certified by peer review) is the author/funder, who has granted bioRxiv a license to display the preprint in perpetuity. It is made available under aCC-BY-ND 4.0 International license.

866 Hashimoto, T., Elder, C.M., Okun, M.S., Patrick, S.K., and Vitek, J.L. (2003). Stimulation of the
867 Subthalamic Nucleus Changes the Firing Pattern of Pallidal Neurons. J Neurosci *23*, 1916–1923.

868 Hegeman, D.J., Hong, E.S., Hernández, V.M., and Chan, C.S. (2016). The external globus
869 pallidus: progress and perspectives. Eur J Neurosci *43*, 1239–1265.

870 Hemptinne, C. de, Swann, N.C., Ostrem, J.L., Ryapolova-Webb, E.S., Luciano, M.S., Galifianakis,
871 N.B., and Starr, P.A. (2015). Therapeutic deep brain stimulation reduces cortical phase-amplitude
872 coupling in Parkinson's disease. Nat Neurosci *18*, 779–786.

873 Herzog, J., Fietzek, U., Hamel, W., Morsnowski, A., Steigerwald, F., Schrader, B., Weinert, D.,
874 Pfister, G., Müller, D., Mehdorn, H.M., et al. (2004). Most effective stimulation site in subthalamic
875 deep brain stimulation for Parkinson's disease. Movement Disord *19*, 1050–1054.

876 Hontanilla, B., Parent, A., Heras, S. de las, and Giménez-Amaya, J.M. (1998). Distribution of
877 calbindin D-28k and parvalbumin neurons and fibers in the rat basal ganglia. Brain Res Bull *47*,
878 107–116.

879 Horn, A., and Kühn, A.A. (2015). Lead-DBS: A toolbox for deep brain stimulation electrode
880 localizations and visualizations. Neuroimage *107*, 127–135.

881 Hu, H., Gan, J., and Jonas, P. (2014). Fast-spiking, parvalbumin^{+} GABAergic interneurons: From
882 cellular design to microcircuit function. Science *345*, 1255263.

883 Huang, C.-S., Wang, G.-H., Tai, C.-H., Hu, C.-C., and Yang, Y.-C. (2017). Antiarrhythmics cure
884 brain arrhythmia: The imperativeness of subthalamic ERG K+ channels in parkinsonian
885 discharges. Sci Adv *3*, e1602272.

886 Hunnicutt, B.J., Jongbloets, B.C., Birdsong, W.T., Gertz, K.J., Zhong, H., and Mao, T. (2016). A
887 comprehensive excitatory input map of the striatum reveals novel functional organization. Elife *5*,
888 e19103.

889 Jinno, S., and Kosaka, T. (2004). Parvalbumin is expressed in glutamatergic and GABAergic
890 corticostriatal pathway in mice. J Comp Neurol *477*, 188–201.

891 Kaku, H., Ozturk, M., Viswanathan, A., Shahed, J., Sheth, S., Kumar, S., and Ince, N.F. (2019).
892 Unsupervised Clustering Reveals Spatially Varying Single Neuronal Firing Patterns in the
893 Subthalamic Nucleus of Patients with Parkinson's Disease. Clin Park Relat Disord *3*, 100032.

894 Karube, F., Takahashi, S., Kobayashi, K., and Fujiyama, F. (2019). Motor cortex can directly drive
895 the globus pallidus neurons in a projection neuron type-dependent manner in the rat. Elife *8*,
896 e49511.

897 Kass, J.I., and Mintz, I.M. (2006). Silent plateau potentials, rhythmic bursts, and pacemaker firing:
898 Three patterns of activity that coexist in quadristable subthalamic neurons. P Natl Acad Sci Usa
899 *103*, 183–188.

900 Kato, S., Kobayashi, K., and Kobayashi, K. (2014). Improved transduction efficiency of a lentiviral
901 vector for neuron-specific retrograde gene transfer by optimizing the junction of fusion envelope
902 glycoprotein. J Neurosci Meth *227*, 151–158.

bioRxiv preprint doi: https://doi.org/10.1101/2021.10.01.462690; this version posted October 1, 2021. The copyright holder for this preprint (which was not certified by peer review) is the author/funder, who has granted bioRxiv a license to display the preprint in perpetuity. It is made available under aCC-BY-ND 4.0 International license.

903 Keuken, M.C., Uylings, H.B.M., Geyer, S., Schäfer, A., Turner, R., and Forstmann, B.U. (2012).
904 Are there three subdivisions in the primate subthalamic nucleus? Front Neuroanat *6*, 14.

905 Kim, H., Paek, S.H., Kim, J., Lee, J., Lim, Y.H., Kim, D.G., and Jeon, B.S. (2009). Two-year
906 follow-up on the effect of unilateral subthalamic deep brain stimulation in highly asymmetric
907 Parkinson's disease. Movement Disord *24*, 329–335.

908 Kim, H.-J., Jeon, B.S., Paek, S.H., Lee, J.-Y., Kim, H.J., Kim, C.K., and Kim, D.G. (2010).
909 Bilateral Subthalamic Deep Brain Stimulation in Parkinson Disease Patients With Severe Tremor.
910 Neurosurgery *67*, 626–632.

911 Kim, H.-J., Jeon, B.S., and Paek, S.H. (2015). Nonmotor Symptoms and Subthalamic Deep Brain
912 Stimulation in Parkinson's Disease. J Mov Disord *8*, 83–91.

913 Kim, J., Zhao, T., Petralia, R.S., Yu, Y., Peng, H., Myers, E., and Magee, J.C. (2012). mGRASP
914 enables mapping mammalian synaptic connectivity with light microscopy. Nat Methods *9*, 96–102.

915 Kita, T., and Kita, H. (2012). The Subthalamic Nucleus Is One of Multiple Innervation Sites for
916 Long-Range Corticofugal Axons: A Single-Axon Tracing Study in the Rat. J Neurosci *32*, 5990–
917 5999.

918 Klein, S., Staring, M., Murphy, K., Viergever, M.A., and Pluim, J.P.W. (2010). elastix: A Toolbox
919 for Intensity-Based Medical Image Registration. Ieee T Med Imaging *29*, 196–205.

920 Kopell, B.H., Rezai, A.R., Chang, J.W., and Vitek, J.L. (2006). Anatomy and physiology of the
921 basal ganglia: Implications for deep brain stimulation for Parkinson's disease. Movement Disord
922 *21*, S238–S246.

923 Kruskal, J., and Wish, M. (1978). Multidimensional Scaling.

924 Kuan, L., Li, Y., Lau, C., Feng, D., Bernard, A., Sunkin, S.M., Zeng, H., Dang, C., Hawrylycz, M.,
925 and Ng, L. (2015). Neuroinformatics of the Allen Mouse Brain Connectivity Atlas. Methods *73*, 4–
926 17.

927 Kühn, A.A., Williams, D., Kupsch, A., Limousin, P., Hariz, M., Schneider, G., Yarrow, K., and
928 Brown, P. (2004). Event-related beta desynchronization in human subthalamic nucleus correlates
929 with motor performance. Brain *127*, 735–746.

930 Kwon, O., Feng, L., Druckmann, S., and Kim, J. (2018). Schaffer collateral inputs to CA1
931 excitatory and inhibitory neurons follow different connectivity rules. J Neurosci *38*, 0155–18.

932 Lambert, C., Zrinzo, L., Nagy, Z., Lutti, A., Hariz, M., Foltynie, T., Draganski, B., Ashburner, J.,
933 and Frackowiak, R. (2012). Confirmation of functional zones within the human subthalamic
934 nucleus: Patterns of connectivity and sub-parcellation using diffusion weighted imaging.
935 Neuroimage *60*, 83–94.

936 Lambert, C., Zrinzo, L., Nagy, Z., Lutti, A., Hariz, M., Foltynie, T., Draganski, B., Ashburner, J.,
937 and Frackowiak, R. (2015). Do we need to revise the tripartite subdivision hypothesis of the
938 human subthalamic nucleus (STN)? Response to Alkemade and Forstmann. Neuroimage *110*, 1–
939 2.

bioRxiv preprint doi: https://doi.org/10.1101/2021.10.01.462690; this version posted October 1, 2021. The copyright holder for this preprint (which was not certified by peer review) is the author/funder, who has granted bioRxiv a license to display the preprint in perpetuity. It is made available under aCC-BY-ND 4.0 International license.

940 Lévesque, J., and Parent, A. (2005). GABAergic interneurons in human subthalamic nucleus.
941 Movement Disord *20*, 574–584.

942 Li, Q., Ke, Y., Chan, D.C.W., Qian, Z.-M., Yung, K.K.L., Ko, H., Arbuthnott, G.W., and Yung, W.-H.
943 (2012). Therapeutic Deep Brain Stimulation in Parkinsonian Rats Directly Influences Motor Cortex.
944 Neuron *76*, 1030–1041.

945 Limousin, P., Pollak, P., Benazzouz, A., Hoffmann, D., Bas, J.-F.L., Perret, J.E., Benabid, A.-L.,
946 and Broussolle, E. (1995). Effect on parkinsonian signs and symptoms of bilateral subthalamic
947 nucleus stimulation. Lancet *345*, 91–95.

948 Lozano, A.M., and Lipsman, N. (2013). Probing and Regulating Dysfunctional Circuits Using
949 Deep Brain Stimulation. Neuron *77*, 406–424.

950 Maier-Hein, K.H., Neher, P.F., Houde, J.-C., Côté, M.-A., Garyfallidis, E., Zhong, J., Chamberland,
951 M., Yeh, F.-C., Lin, Y.-C., Ji, Q., et al. (2017). The challenge of mapping the human connectome
952 based on diffusion tractography. Nat Commun *8*, 1349.

953 Mallet, L., Schüpbach, M., N'Diaye, K., Remy, P., Bardinet, E., Czernecki, V., Welter, M.-L.,
954 Pelissolo, A., Ruberg, M., Agid, Y., et al. (2007). Stimulation of subterritories of the subthalamic
955 nucleus reveals its role in the integration of the emotional and motor aspects of behavior. Proc
956 National Acad Sci *104*, 10661–10666.

957 Mallet, N., Micklem, B.R., Henny, P., Brown, M.T., Williams, C., Bolam, J.P., Nakamura, K.C.,
958 and Magill, P.J. (2012). Dichotomous Organization of the External Globus Pallidus. Neuron *74*,
959 1075–1086.

960 Mastro, K.J., Bouchard, R.S., Holt, H.A.K., and Gittis, A.H. (2014). Transgenic Mouse Lines
961 Subdivide External Segment of the Globus Pallidus (GPe) Neurons and Reveal Distinct GPe
962 Output Pathways. J Neurosci *34*, 2087–2099.

963 Mastro, K.J., Zitelli, K.T., Willard, A.M., Leblanc, K.H., Kravitz, A.V., and Gittis, A.H. (2017). Cell-
964 specific pallidal intervention induces long-lasting motor recovery in dopamine-depleted mice. Nat
965 Neurosci *20*, 815–823.

966 Monakow, K.H., Akert, K., and Künzle, H. (1978). Projections of the precentral motor cortex and
967 other cortical areas of the frontal lobe to the subthalamic nucleus in the monkey. Exp Brain Res
968 *33*, 395–403.

969 Mosher, C.P., Mamelak, A.N., Malekmohammadi, M., Pouratian, N., and Rutishauser, U. (2021).
970 Distinct roles of dorsal and ventral subthalamic neurons in action selection and cancellation.
971 Neuron *109*, 869-881.e6.

972 Mukherjee, A., Bajwa, N., Lam, N.H., Porrero, C., Clasca, F., and Halassa, M.M. (2020). Variation
973 of connectivity across exemplar sensory and associative thalamocortical loops in the mouse. Elife
974 *9*, e62554.

975 Naito, A., and Kita, H. (1994). The cortico-pallidal projection in the rat: an anterograde tracing
976 study with biotinylated dextran amine. Brain Res *653*, 251–257.

bioRxiv preprint doi: https://doi.org/10.1101/2021.10.01.462690; this version posted October 1, 2021. The copyright holder for this preprint (which was not certified by peer review) is the author/funder, who has granted bioRxiv a license to display the preprint in perpetuity. It is made available under aCC-BY-ND 4.0 International license.

977 Nambu, A., Tokuno, H., and Takada, M. (2002). Functional significance of the cortico–
978 subthalamo–pallidal 'hyperdirect' pathway. Neurosci Res *43*, 111–117.

979 Oh, S., Chung, J., In, M., Zaitsev, M., Kim, Y., Speck, O., and Cho, Z. (2012). Distortion
980 correction in EPI at ultra-high-field MRI using PSF mapping with optimal combination of shift
981 detection dimension. Magnet Reson Med *68*, 1239–1246.

982 Oh, S.W., Harris, J.A., Ng, L., Winslow, B., Cain, N., Mihalas, S., Wang, Q., Lau, C., Kuan, L.,
983 Henry, A.M., et al. (2014). A mesoscale connectome of the mouse brain. Nature *508*, 207–214.

984 Paek, S.H., Han, J.H., Lee, J.-Y., Kim, C., Jeon, B.S., and Kim, D.G. (2008). Electrode Position
985 Determined by Fused Images of Preoperative and Postoperative Magnetic Resonance Imaging
986 and Surgical Outcome after Subthalamic Nucleus Deep Brain Stimulation. Neurosurgery *63*, 925–
987 937.

988 Parent, A., and Hazrati, L.-N. (1995). Functional anatomy of the basal ganglia. II. The place of
989 subthalamic nucleus and external pallidium in basal ganglia circuitry. Brain Res Rev *20*, 128–154.

990 Peng, T., Thorn, K., Schroeder, T., Wang, L., Theis, F.J., Marr, C., and Navab, N. (2017). A
991 BaSiC tool for background and shading correction of optical microscopy images. Nat Commun *8*,
992 14836.

993 Petersen, M.V., Mlakar, J., Haber, S.N., Parent, M., Smith, Y., Strick, P.L., Griswold, M.A., and
994 McIntyre, C.C. (2019). Holographic Reconstruction of Axonal Pathways in the Human Brain.
995 Neuron *104*, 1056-1064.e3.

996 Plantinga, B.R., Roebroeck, A., Kemper, V.G., Uludağ, K., Melse, M., Mai, J., Kuijf, M.L., Herrler,
997 A., Jahanshahi, A., Romeny, B.M. ter H., et al. (2016). Ultra-High Field MRI Post Mortem
998 Structural Connectivity of the Human Subthalamic Nucleus, Substantia Nigra, and Globus
999 Pallidus. Front Neuroanat *10*, 66.

1000 Plantinga, B.R., Temel, Y., Duchin, Y., Uludağ, K., Patriat, R., Roebroeck, A., Kuijf, M.,
1001 Jahanshahi, A., Romenij, B. ter H., Vitek, J., et al. (2018). Individualized parcellation of the
1002 subthalamic nucleus in patients with Parkinson's disease with 7T MRI. Neuroimage *168*, 403–411.

1003 Roccaro-Waldmeyer, D.M., Girard, F., Milani, D., Vannoni, E., Prétôt, L., Wolfer, D.P., and Celio,
1004 M.R. (2018). Eliminating the VGlut2-Dependent Glutamatergic Transmission of Parvalbumin-
1005 Expressing Neurons Leads to Deficits in Locomotion and Vocalization, Decreased Pain
1006 Sensitivity, and Increased Dominance. Front Behav Neurosci *12*, 146.

1007 Schaltenbrand, G., and Wahren, W. (1998). Atlas for Stereotaxy of the Human Brain (Stuttgart
1008 Thieme).

1009 Shang, C., Liu, Z., Chen, Z., Shi, Y., Wang, Q., Liu, S., Li, D., and Cao, P. (2015). A parvalbumin-
1010 positive excitatory visual pathway to trigger fear responses in mice. Science *348*, 1472–1477.

1011 Smith, Y., Bevan, M.D., Shink, E., and Bolam, J.P. (1998). Microcircuitry of the direct and indirect
1012 pathways of the basal ganglia. Neuroscience *86*, 353–387.

bioRxiv preprint doi: https://doi.org/10.1101/2021.10.01.462690; this version posted October 1, 2021. The copyright holder for this preprint (which was not certified by peer review) is the author/funder, who has granted bioRxiv a license to display the preprint in perpetuity. It is made available under aCC-BY-ND 4.0 International license.

1013 Song, J.H., Lucaci, D., Calangiu, I., Brown, M.T.C., Park, J.S., Kim, J., Brickley, S.G., and
1014 Chadderton, P. (2018). Combining mGRASP and Optogenetics Enables High-Resolution
1015 Functional Mapping of Descending Cortical Projections. Cell Reports *24*, 1071–1080.

1016 Stefani, A., Fedele, E., Galati, S., Pepicelli, O., Frasca, S., Pierantozzi, M., Peppe, A., Brusa, L.,
1017 Orlacchio, A., Hainsworth, A.H., et al. (2005). Subthalamic stimulation activates internal pallidus:
1018 Evidence from cGMP microdialysis in PD patients. Ann Neurol *57*, 448–452.

1019 Steigerwald, F., Po□tter, M., Herzog, J., Pinsker, M., Kopper, F., Mehdorn, H., Deuschl, G., and
1020 Volkmann, J. (2008). Neuronal Activity of the Human Subthalamic Nucleus in the Parkinsonian
1021 and Nonparkinsonian State. J Neurophysiol *100*, 2515–2524.

1022 Tervo, D.G.R., Hwang, B.-Y., Viswanathan, S., Gaj, T., Lavzin, M., Ritola, K.D., Lindo, S., Michael,
1023 S., Kuleshova, E., Ojala, D., et al. (2016). A Designer AAV Variant Permits Efficient Retrograde
1024 Access to Projection Neurons. Neuron *92*, 372–382.

1025 Tomer, R., Ye, L., Hsueh, B., and Deisseroth, K. (2014). Advanced CLARITY for rapid and high-
1026 resolution imaging of intact tissues. Nat Protoc *9*, 1682–1697.

1027 Tournier, J.-D., Calamante, F., and Connelly, A. (2010). Improved probabilistic streamlines
1028 tractography by 2 order integration over fibre orientation distributions Proc. Intl. S. Proc. Intl. Soc.
1029 Mag. Reson. Med *18*.

1030 Turrigiano, G. (2011). Too Many Cooks? Intrinsic and Synaptic Homeostatic Mechanisms in
1031 Cortical Circuit Refinement. Neuroscience *34*, 89–103.

1032 Wallace, M.L., Saunders, A., Huang, K.W., Philson, A.C., Goldman, M., Macosko, E.Z., McCarroll,
1033 S.A., and Sabatini, B.L. (2017). Genetically Distinct Parallel Pathways in the Entopeduncular
1034 Nucleus for Limbic and Sensorimotor Output of the Basal Ganglia. Neuron *94*, 138-152.e5.

1035 Wang, Q., Ding, S.-L., Li, Y., Royall, J., Feng, D., Lesnar, P., Graddis, N., Naeemi, M., Facer, B.,
1036 Ho, A., et al. (2020). The Allen Mouse Brain Common Coordinate Framework: A 3D Reference
1037 Atlas. Cell *181*, 936-953.e20.

1038 Windels, F., Bruet, N., Poupard, A., Urbain, N., Chouvet, G., Feuerstein, C., and Savasta, M.
1039 (2000). Effects of high frequency stimulation of subthalamic nucleus on extracellular glutamate
1040 and GABA in substantia nigra and globus pallidus in the normal rat. Eur J Neurosci *12*, 4141–
1041 4146.

1042 Winnubst, J., Bas, E., Ferreira, T.A., Wu, Z., Economo, M.N., Edson, P., Arthur, B.J., Bruns, C.,
1043 Rokicki, K., Schauder, D., et al. (2019). Reconstruction of 1,000 Projection Neurons Reveals New
1044 Cell Types and Organization of Long-Range Connectivity in the Mouse Brain. Cell *179*, 268-
1045 281.e13.

1046 Wodarg, F., Herzog, J., Reese, R., Falk, D., Pinsker, M.O., Steigerwald, F., Jansen, O., Deuschl,
1047 G., Mehdorn, H.M., and Volkmann, J. (2012). Stimulation site within the MRI-defined STN
1048 predicts postoperative motor outcome. Movement Disord *27*, 874–879.

1049 Wu, X.H., Song, J.J., Faull, R.L.M., and Waldvogel, H.J. (2018). GABAA and GABAB receptor
1050 subunit localization on neurochemically identified neurons of the human subthalamic nucleus. J
1051 Comp Neurol *526*, 803–823.

bioRxiv preprint doi: https://doi.org/10.1101/2021.10.01.462690; this version posted October 1, 2021. The copyright holder for this preprint (which was not certified by peer review) is the author/funder, who has granted bioRxiv a license to display the preprint in perpetuity. It is made available under aCC-BY-ND 4.0 International license.

1052 Yizhar, O., Fenno, L.E., Prigge, M., Schneider, F., Davidson, T.J., O'Shea, D.J., Sohal, V.S.,
1053 Goshen, I., Finkelstein, J., Paz, J.T., et al. (2011). Neocortical excitation/inhibition balance in
1054 information processing and social dysfunction. Nature *477*, 171–178.

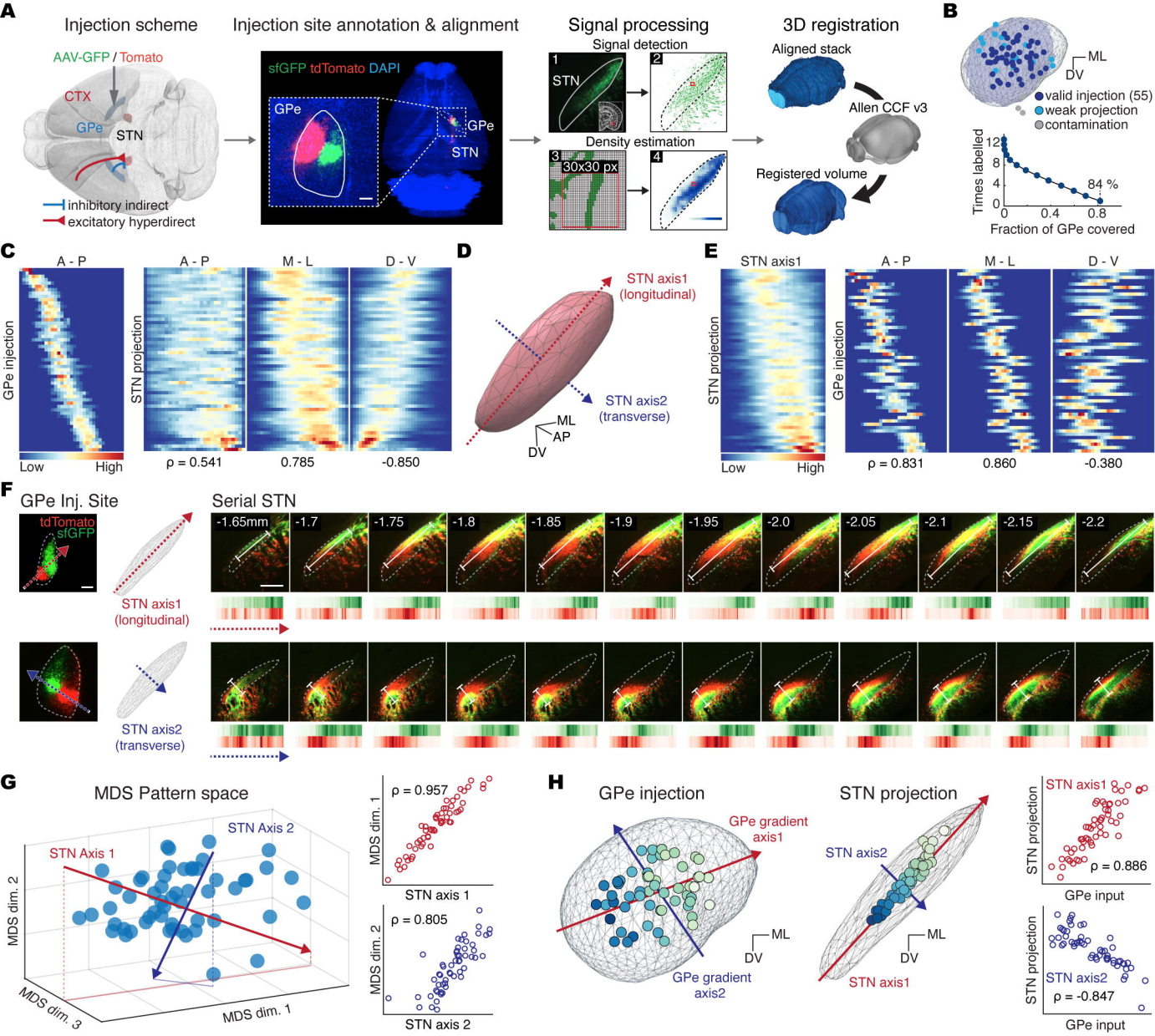
A
Injection scheme
AAV-GFP / Tomato
CTX
GPe
STN
inhibitory indirect
excitatory hyperdirect
Injection site annotation & alignment
sfGFP tdTomato DAPI
GPe
STN
Signal processing
Signal detection
Density estimation
30x30 px
3D registration
Aligned stack
Allen CCF v3
Registered volume
B
ML
DV
valid injection (55)
weak projection
contamination
Times labelled
84 %
Fraction of GPe covered
C
A - P
M - L
D - V
GPe injection
STN projection
Low
High
ρ = 0.541
0.785
-0.850
D
STN axis1
(longitudinal)
STN axis2
(transverse)
ML
AP
DV
E
STN axis1
STN projection
GPe injection
ρ = 0.831
0.860
-0.380
F
GPe Inj. Site
tdTomato
sfGFP
Serial STN
-1.65mm
-1.7
-1.75
-1.8
-1.85
-1.9
-1.95
-2.0
-2.05
-2.1
-2.15
-2.2
STN axis1
(longitudinal)
STN axis2
(transverse)
G
MDS Pattern space
STN Axis 1
STN Axis 2
MDS dim. 1
MDS dim. 2
MDS dim. 3
ρ = 0.957
STN axis 1
ρ = 0.805
STN axis 2
H
GPe injection
GPe gradient
axis1
GPe gradient
axis2
ML
DV
STN projection
STN axis2
STN axis1
STN axis1
ρ = 0.886
GPe input
STN axis2
ρ = -0.847
GPe input

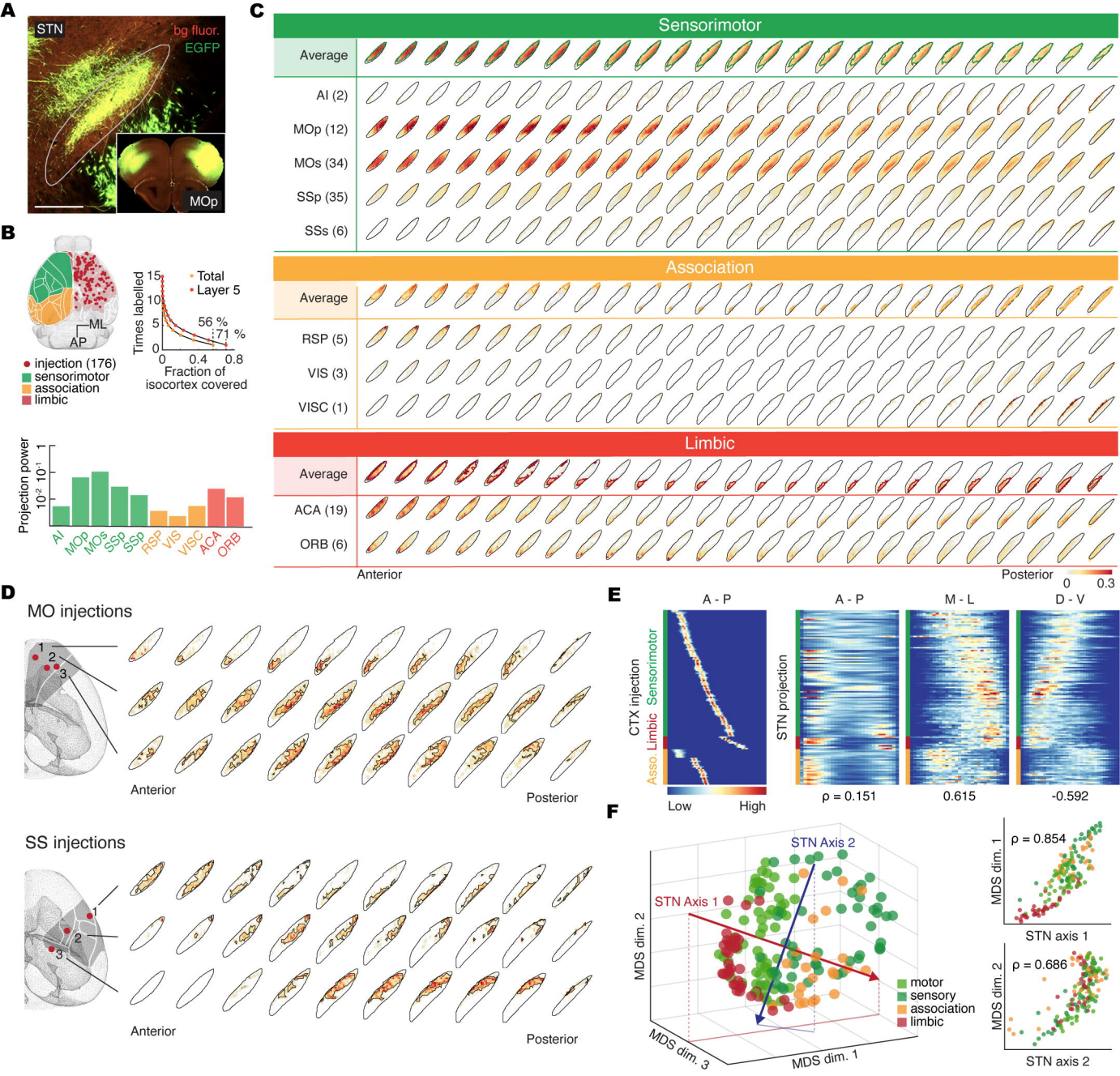
A
STN
bg fluor.
EGFP
MOp
B
ML
AP
injection (176)
sensorimotor
association
limbic
Times labelled
Total
Layer 5
56 %
71 %
Fraction of isocortex covered
Projection power
AI
MOp
MOs
SSp
SSp
RSP
VIS
VISC
ACA
ORB
C
Sensorimotor
Average
AI (2)
MOp (12)
MOs (34)
SSp (35)
SSs (6)
Association
Average
RSP (5)
VIS (3)
VISC (1)
Limbic
Average
ACA (19)
ORB (6)
Anterior
Posterior
0
0.3
D
MO injections
Anterior
Posterior
SS injections
Anterior
Posterior
E
A - P
A - P
M - L
D - V
CTX injection
Sensorimotor
Asso.
Limbic
STN projection
Low
High
ρ = 0.151
0.615
-0.592
F
STN Axis 2
STN Axis 1
MDS dim. 2
MDS dim. 3
MDS dim. 1
motor
sensory
association
limbic
ρ = 0.854
MDS dim. 1
STN axis 1
ρ = 0.686
MDS dim. 2
STN axis 2

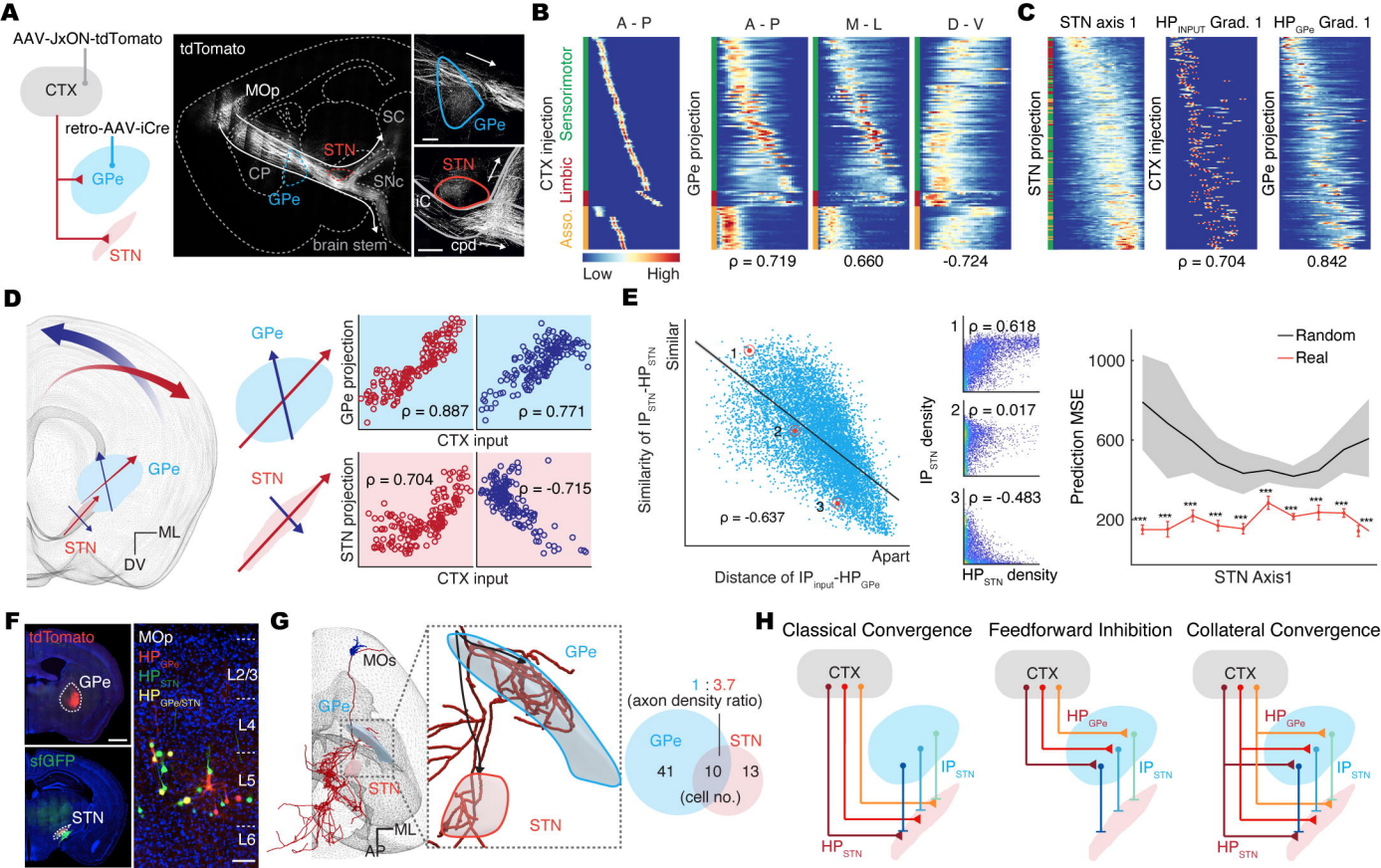
A
AAV-JxON-tdTomato
CTX
retro-AAV-iCre
GPe
STN
tdTomato
MOp
SC
STN
CP
GPe
SNc
brain stem
GPe
STN
iC
cpd
B
A - P
A - P
M - L
D - V
CTX injection
Sensorimotor
Limbic
Asso.
GPe projection
Low
High
ρ = 0.719
0.660
-0.724
C
STN axis 1
HP$_{INPUT}$ Grad. 1
HP$_{GPe}$ Grad. 1
STN projection
CTX injection
GPe projection
ρ = 0.704
0.842
D
GPe
STN
ML
DV
GPe
STN
GPe projection
ρ = 0.887
ρ = 0.771
CTX input
STN projection
ρ = 0.704
ρ = -0.715
CTX input
E
Similarity of IP$_{STN}$-HP$_{STN}$
Similar
Apart
Distance of IP$_{input}$-HP$_{GPe}$
ρ = -0.637
1
2
3
IP$_{STN}$ density
ρ = 0.618
ρ = 0.017
ρ = -0.483
HP$_{STN}$ density
Random
Real
Prediction MSE
1000
600
200
STN Axis1
F
tdTomato
GPe
sfGFP
STN
MOp
HP$_{GPe}$
HP$_{STN}$
HP$_{GPe/STN}$
L2/3
L4
L5
L6
G
MOs
GPe
STN
ML
AP
GPe
STN
1 : 3.7
(axon density ratio)
GPe
STN
41
10
13
(cell no.)
H
Classical Convergence
Feedforward Inhibition
Collateral Convergence
CTX
HP$_{STN}$
IP$_{STN}$
HP$_{GPe}$

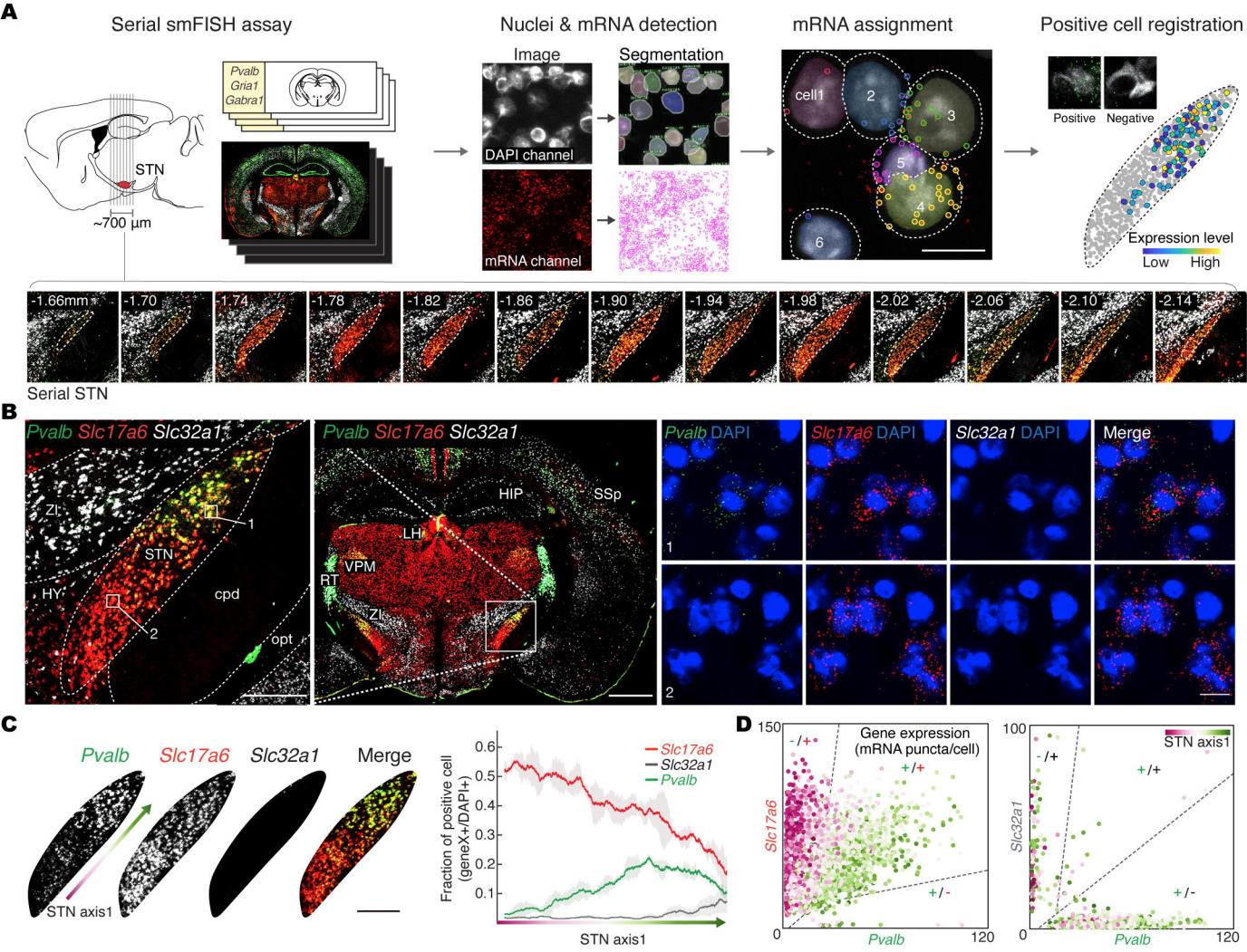
A
Serial smFISH assay
Nuclei & mRNA detection
mRNA assignment
Positive cell registration
STN
~700 µm
Pvalb
Gria1
Gabra1
Image
Segmentation
DAPI channel
mRNA channel
cell1
2
3
4
5
6
Positive
Negative
Expression level
Low
High
-1.66mm
-1.70
-1.74
-1.78
-1.82
-1.86
-1.90
-1.94
-1.98
-2.02
-2.06
-2.10
-2.14
Serial STN
B
Pvalb Slc17a6 Slc32a1
ZI
STN
HY
cpd
opt
HIP
SSp
LH
VPM
RT
Pvalb DAPI
Slc17a6 DAPI
Slc32a1 DAPI
Merge
C
Pvalb
Slc17a6
Slc32a1
Merge
STN axis1
Fraction of positive cell (geneX+/DAPI+)
STN axis1
D
Gene expression (mRNA puncta/cell)
Slc17a6
Pvalb
Slc32a1
STN axis1

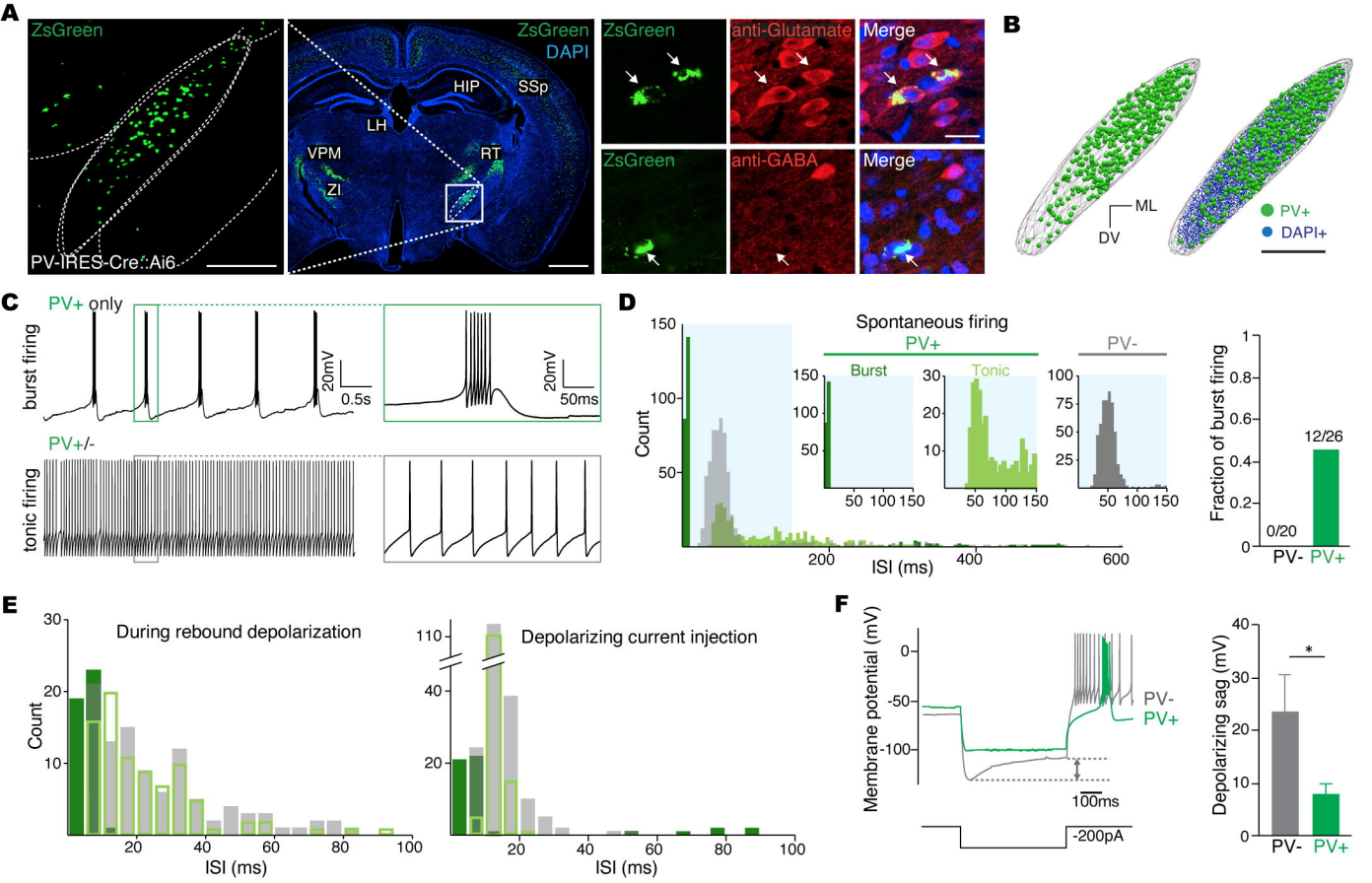
A
ZsGreen
PV-IRES-Cre::Ai6
ZsGreen
DAPI
HIP
SSp
LH
VPM
RT
ZI
ZsGreen
anti-Glutamate
Merge
ZsGreen
anti-GABA
Merge
B
ML
DV
PV+
DAPI+
C
PV+ only
burst firing
20mV
0.5s
20mV
50ms
PV+/-
tonic firing
D
Spontaneous firing
PV+
PV-
Burst
Tonic
Count
ISI (ms)
Fraction of burst firing
0/20
12/26
PV-
PV+
E
During rebound depolarization
Depolarizing current injection
Count
ISI (ms)
ISI (ms)
F
Membrane potential (mV)
PV-
PV+
100ms
-200pA
Depolarizing sag (mV)
*
PV-
PV+

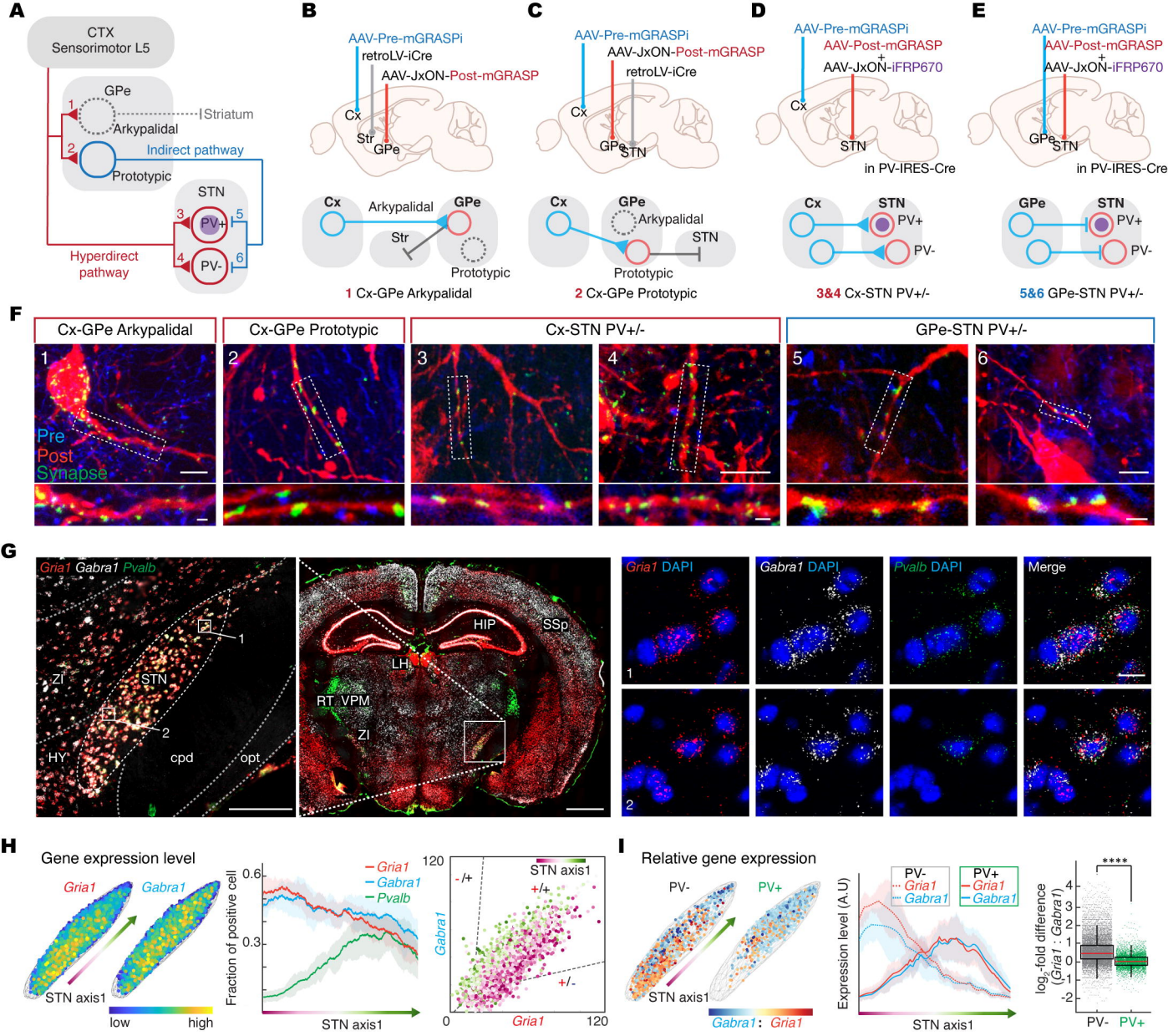
A
CTX
Sensorimotor L5
GPe
Striatum
Arkypalidal
Indirect pathway
Prototypic
STN
PV+
PV-
Hyperdirect
pathway
B
AAV-Pre-mGRASPi
retroLV-iCre
AAV-JxON-Post-mGRASP
Cx
Str
GPe
Arkypalidal
Prototypic
1 Cx-GPe Arkypalidal
C
AAV-Pre-mGRASPi
AAV-JxON-Post-mGRASP
retroLV-iCre
Cx
GPe
STN
Arkypalidal
Prototypic
2 Cx-GPe Prototypic
D
AAV-Pre-mGRASPi
AAV-Post-mGRASP
+
AAV-JxON-iFRP670
Cx
STN
in PV-IRES-Cre
PV+
PV-
3&4 Cx-STN PV+/-
E
AAV-Pre-mGRASPi
AAV-Post-mGRASP
+
AAV-JxON-iFRP670
GPe
STN
in PV-IRES-Cre
5&6 GPe-STN PV+/-
F
Cx-GPe Arkypalidal
Cx-GPe Prototypic
Cx-STN PV+/-
GPe-STN PV+/-
Pre
Post
Synapse
G
Gria1 Gabra1 Pvalb
ZI
STN
HY
cpd
opt
HIP
SSp
LH
RT
VPM
Gria1 DAPI
Gabra1 DAPI
Pvalb DAPI
Merge
H
Gene expression level
Gria1
Gabra1
STN axis1
low
high
Fraction of positive cell
Pvalb
-/+
+/+
+/-
I
Relative gene expression
PV-
PV+
Gabra1 : Gria1
Expression level (A.U)
log2-fold difference (Gria1 : Gabra1)
****

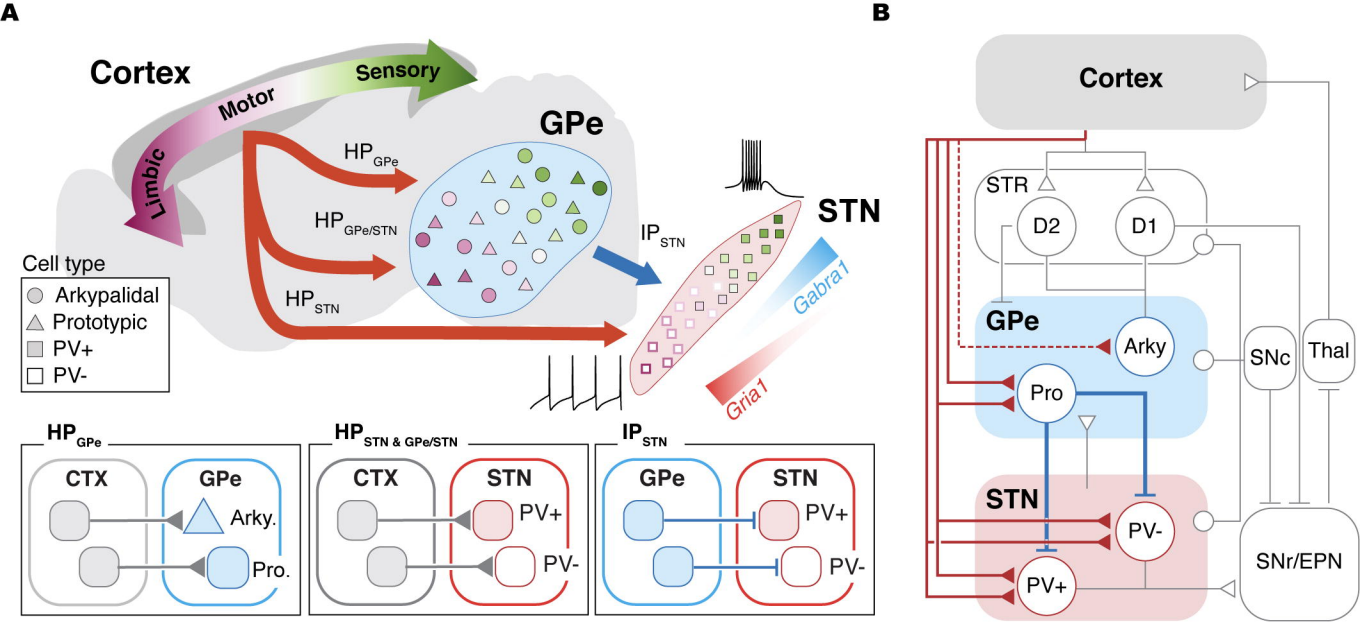
A
Cortex
Motor
Sensory
Limbic
GPe
HP GPe
HP GPe/STN
HP STN
IP STN
STN
Gabra1
Gria1
Cell type
Arkypalidal
Prototypic
PV+
PV-
HP GPe
CTX
GPe
Arky.
Pro.
HP STN & GPe/STN
CTX
STN
PV+
PV-
IP STN
GPe
STN
PV+
PV-
B
Cortex
STR
D2
D1
GPe
Arky
Pro
SNc
Thal
STN
PV-
PV+
SNr/EPN